Natland, J.H., Dick H.J.B., Miller, D.J., and Von Herzen, R.P. (Eds.)
Proceedings of the Ocean Drilling Program, Scientific Results Volume 176

4. High-Temperature Fluid Migration within Oceanic Layer 3 Gabbros, Hole 735B, Southwest Indian Ridge: Implications for the Magmatic–Hydrothermal Transition at Slow-Spreading Mid-Ocean Ridges[1]

Jinichiro Maeda,[2] H.R. Naslund,[3] Y.D. Jang,[3] Eiichi Kikawa,[4] Takahiro Tajima,[2] and W.H. Blackburn[3]

[1]Maeda, J., Naslund, H.R., Jang, Y.D., Kikawa, E., Tajima, T., and Blackburn, W.H., 2002. High-temperature fluid migration within oceanic Layer 3 gabbros, Hole 735B, Southwest Indian Ridge: implications for the magmatic–hydrothermal transition at slow-spreading mid-ocean ridges. *In* Natland, J.H., Dick, H.J.B., Miller, D.J., and Von Herzen, R.P. (Eds.), *Proc. ODP, Sci. Results,* 176, 1–56 [Online]. Available from World Wide Web: <http://www-odp. tamu.edu/publications/176_SR/VOLUME/CHAPTERS/SR176_04.PDF>. [Cited YYYY-MM-DD]
[2]Division of Earth and Planetary Sciences, Graduate School of Science, Hokkaido University, N10 W8 Kita, Sapporo, Hokkaido 060-0810, Japan. Correspondence author: **jinmaeda@ep.sci.hokudai.ac.jp**
[3]Department of Geological Sciences and Environmental Studies, State University of New York, Binghamton NY 13902-6000, USA.
[4]Global Environmental Laboratory, University of Toyama, 3190 Gofuku, Toyama 930, Japan. Present address: Deep Sea Research Department, Japan Marine Science and Technology Center, 2-15 Natsushima-cho, Yokosuka 237-0061, Japan.

Initial receipt: 6 July 2000
Acceptance: 12 September 2001
Web publication: 26 February 2002
Ms 176SR-004

ABSTRACT

The transition from magmatic crystallization to high-temperature metamorphism in deep magma chambers (or lenses) beneath spreading ridges has not been fully described. High-temperature microscopic veins found in olivine gabbros, recovered from Ocean Drilling Program Hole 735B on the Southwest Indian Ridge during Leg 176, yield information on the magmatic–hydrothermal transition beneath spreading ridges. The microscopic veins are composed of high-temperature minerals, (i.e., clinopyroxene, orthopyroxene, brown amphibole, and plagioclase). An important feature of these veins is the "along-vein variation" in mineralogy, which is correlated with the magmatic minerals that they penetrate. Within grains of magmatic plagioclase, the veins are composed of less calcic plagioclase. In grains of olivine, the veins are composed of orthopyroxene + brown amphibole + plagioclase. In clinopyroxene grains, the veins consist of plagioclase + brown amphibole and are accompanied by an intergrowth of brown amphibole + orthopyroxene. The mode of occurrence of the veins cannot be explained if these veins were crystallized from silicate melts. Consequently, these veins and nearby intergrowths were most likely formed by the reaction of magmatic minerals with fluid phases under the conditions of low

fluid/rock ratios. Very similar intergrowths of brown amphibole + orthopyroxene are observed in clinopyroxene grains with "interfingering" textures. It is believed, in general, that the penetration of seawater does not predate the ductile deformation within Layer 3 gabbros of the slow-spreading ridges. If this is the case, the fluid responsible for the veins did not originate from seawater because the formation of the veins and the interfingering textures preceded ductile deformation and, perhaps, complete solidification of the gabbroic crystal mush. It has been proposed, based on fluid inclusion data, that the exsolution of fluid from the latest-stage magma took place at temperatures >700°C in the slow-spreading Mid-Atlantic Ridge at the Kane Fracture Zone (MARK) area. No obvious mineralogical evidence, however, has been found for these magmatic fluids. The calculated temperatures for the veins and nearby intergrowths found in Hole 735B gabbros are up to 1000°C, and these veins are the most plausible candidate for the mineralogical expression of the migrating magmatic fluids.

INTRODUCTION

Oceanic crusts are formed by an integrated process that includes upwelling and partial melting of asthenospheric mantle, generation, segregation, emplacement, and crystallization of primitive basaltic magma, and subsequent metamorphism, alteration, and tectonic deformation. The transition from magmatic to metamorphic processes takes place in magma chambers beneath spreading ridges with decreasing temperature and with incorporation of hydrothermal fluids. It is widely accepted that the hydrothermal circulation of seawater results in heat flow anomalies, metamorphism, and the formation of metalliferous ore deposits. These processes are very important to understanding heat flux and geochemical cycling between oceanic lithosphere and hydrosphere (e.g., Gillis et al., 1993; Kelley et al., 1993; Mével and Cannat, 1991; Cannat et al., 1991; Pflumio, 1991; Schiffman et al., 1991; Manning et al., 1996; Gillis and Roberts, 1999; Talbi et al., 1999). On the other hand, the transition from magmatic to metamorphic/hydrothermal processes is likely to depend on the spreading rate of ridges where the spreading rate has an effect on the thermal regime of the spreading ridges. However, the transition in deep magma chambers has not been described in detail from various settings with different spreading rates. So it is one of the most important subjects to be examined in the long section of oceanic crust drilled in Hole 735B, Atlantis II Fracture Zone, on the Southwest Indian Ridge. Here, we describe a type of high-temperature microscopic vein from olivine gabbros. This type of vein provides a line of evidence for the earliest migration of fluids in the deep magma chambers in the lower oceanic crust of the slow-spreading Southwest Indian Ridge.

GEOLOGIC SETTING AND LITHOLOGIC FRAMEWORK OF HOLE 735B

Hole 735B (32°43.39′S, 57°15.96′E) is located on the eastern flank of the Atlantis II Fracture Zone of the Southwest Indian Ridge. This part of the oceanic crust was formed at ~11 Ma beneath the Southwest Indian Ridge at a very slow half-spreading rate of 8 mm/yr (Fisher and Sclater, 1983; Dick et al., 2000). Coarse-grained lower crustal gabbros and man-

tle peridotites are predominantly exposed on a wave-cut terrace (Atlantis Bank) at a water depth of 700 m along a transverse ridge of the Atlantis II Fracture Zone (Dick et al., 1991b). Hole 735B is situated on this bank and was originally drilled ~500 m during Leg 118 in 1987 and was deepened to 1508 meters below seafloor (mbsf) in 1997 during Leg 176. The entire core drilled during these two legs is composed of crustal lithologies, and no mantle peridotite was sampled. Oceanic Layer 3 around this site is believed to be ~2 km thick (Muller et al., 1997). Therefore, the 1500-m-long section of Layer 3 gabbro with an exceptionally high recovery rate (~86%) from Hole 735B may provide us with one of the best opportunities for understanding the architecture and evolution of the oceanic crust, especially that formed at very slow-spreading ridges.

The major lithologic units in Hole 735B core include troctolite, olivine gabbro, gabbro, and gabbronorite. These show coarse-grained equigranular texture, in general, and constitute >90 vol% of the recovered core. Subordinate lithologic units cored during Leg 176 include microgabbros, oxide-rich gabbros, and felsic rocks. The microgabbros show equigranular, fine-grained textures and are observed as veins and dikelets intruding the olivine gabbros. The microgabbros appear to represent channels through which silicate melt migrated to the upper portion of the crust. Their compositions range from troctolite through olivine gabbro to oxide-rich gabbro and, in general, do not represent magmatic compositions in spite of their fine-grained textures (e.g., Dick, Natland, Miller, et al., 1999). The oxide-rich gabbros range in composition from oxide-rich troctolite through oxide-rich olivine gabbro to oxide-rich gabbros. The oxide-rich gabbros intrude into the olivine gabbros as dikes and veins usually associated with strong ductile deformation (e.g., Cannat, 1991). The felsic rocks are present as veins and dikelets and are dioritic, trondhjemitic, tonalitic, and granitic in composition. The felsic rocks include a diverse suite that may have originated from magmatic and hydrothermal processes. More detailed petrographical descriptions of the core recovered from Hole 735B are given in Dick, Natland, Miller, et al. (1999) and Robinson, Von Herzen, et al. (1989).

For the full depth of Hole 735B drilled during Legs 118 and 176, 12 major lithologic units were identified based on modal mineralogy and the relative abundance of rock types (Dick et al., 1991a, 2000; Dick, Natland, Miller, et al., 1999). The downhole sequence can be also subdivided into several units based on the whole-rock major element chemistry of the dominant lithologic unit, the olivine gabbros. Dick, Natland, Miller, et al. (1999) and Dick et al. (2000) recognized five units of ~200–300 m thickness. Each unit has a coherent chemical variation assumed for magmatic fractionation (e.g., see Fig. **F1**). This variation corresponds to a lithologic change from troctolite through olivine gabbro to gabbro and gabbronorite. These chemically defined units may represent an individual magmatic batch supplied by small and ephemeral magma chambers beneath the Southwest Indian Ridge (Dick, Natland, Miller, et al., 1999; Dick et al., 2000). Overall, there is no evidence for a large steady-state magma chamber in this downhole sequence.

Several kinds of veins have been described in cores from Hole 735B. In general, these veins are subdivided into two major categories, one crystallized from silicate melts and another the so-called hydrothermal or alteration veins. Clearly classified into the former magmatic veins are the microgabbros, oxide-rich gabbros, and also some trondhjemitic rocks (Stakes et al., 1991). Other veins are related to fluid migration and

F1. Downhole distributions of microscopic veins and interfingering clinopyroxene textures, p. 22.

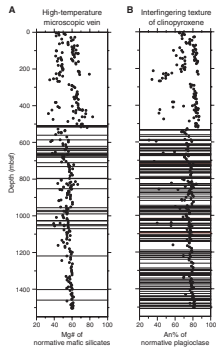

hydrothermal activity during metamorphic processes (e.g., Robinson, Von Herzen, et al., 1989; Robinson et al., 1991; Stakes et al., 1991; Magde et al., 1995). They include amphibole veins, plagioclase + amphibole veins, felsic veins of ambiguous origin, plagioclase + Ca-rich clinopyroxene (clinopyroxene, hereafter) veins, and other veins consisting of very low temperature minerals, such as clay minerals and carbonates (e.g., Magde et al., 1995). Information on the hydrothermal processes was also provided by fluid inclusions and oxygen, Sr, and Nd isotopic studies (e.g., Vanko and Stakes, 1991; Stakes et al., 1991; Kempton et al., 1991; Hart et al., 1999; Kelley and Früh-Green, 1999, in press).

PROBLEMS WITH MAGMATIC/METAMORPHIC TRANSITION BENEATH SPREADING RIDGES

Metamorphism and hydrothermal processes in axial magma chambers have been discussed with special reference to different spreading rates (e.g., Ito and Anderson, 1983; Mével and Cannat, 1991). According to the proposal of Mével and Cannat (1991), axial faults caused by lithospheric stretching extend into the lower crustal magma chambers in slow-spreading ridges. Through the high-temperature ductile shear zones formed by the axial faults, seawater penetration occurs under higher temperature (granulite and/or high amphibolite facies) conditions of >800°C. With cooling and an increase in penetrating seawater, metamorphic hydration proceeds into lower-temperature (greenschist facies and amphibolite/greenschist transitional) conditions. These synkinematic processes are followed by metamorphism under static conditions in which seawater penetrates through brittle failure at ~500°C. In contrast, there is no evidence for axial faults and high-temperature ductile shearing in deep crust at fast-spreading ridges (e.g., Hess Deep on the East Pacific Rise) (Gillis, 1995; Manning and MacLeod, 1996; MacLeod et al., 1996). Consequently, hydrothermal circulation and resultant metamorphism start with downward propagation of a cracking front caused by thermal contraction (Lister, 1974; Mével and Cannat, 1991). Thus, it has been thought that compared with slow-spreading ridges, the onset of metamorphism and hydrothermal penetration at fast-spreading ridges is later and under lower-temperature conditions of ~500°C (Mével and Cannat, 1991). However, Manning and MacLeod (1996) showed that the highest temperature recorded in the earliest amphibole veins is ~600°–750°C in the Hess Deep crust. So it is not clear whether the temperature of initial penetration of seawater is controlled by the difference in the spreading rate or whether these temperatures are higher in slow-spreading ridges than in fast-spreading ridges. Furthermore, fluid inclusion studies have revealed the exsolution of fluids from late-stage magmas at higher temperatures (>700°C) in oceanic gabbros of the slow-spreading Mid-Atlantic Ridge (Kelley and Delaney, 1987; Kelley et al., 1993; Gillis et al., 1993; Kelley, 1996, 1997). So it is necessary to distinguish the fluid phases of seawater origin and those of magmatic origin. On the other hand, based on thermodynamic calculations, McCollom and Shock (1998) mentioned a possibility that seawater circulation commenced at 750°–900°C with no mineralogical expression left in the oceanic gabbros, that is "cryptic alteration." Hart et al. (1999) pointed out that although the isotopic evidence for seawater circulation in Hole 735B gabbros is clear, magmatic effects dominate the trace element signatures.

In this context, the problem that should be addressed is what kind of mineral(s) are the expression of the earliest and highest-temperature metamorphism, and also, what kind of mineral(s) represents the earliest penetration of seawater and/or exsolution of magmatic fluids. Although it is not the purpose of this paper, the origin of amphibole, especially Ti- and Al-rich brown pargasitic amphibole, is one of the most critical problems for such a discussion of the magmatic/hydrothermal transition (e.g., Gillis, 1996; Tribuzio et al., 2000). Chemical composition of amphibole is sensitive to pressure, temperature, and other physical conditions and also to the chemistry of magmas, fluids, or protoliths from which the amphibole was formed. Therefore, in general, it is expected that the composition of amphibole will provide clues about its origin (e.g., Robinson et al., 1982). It is widely accepted that the origin of amphiboles contained in oceanic gabbros is very diverse, and amphiboles of magmatic, subsolidus metamorphic, and hydrothermal origin are included even in a single thin section. Actually, it is not easy to determine the origin of individual amphibole grains based on shape, texture, color, or chemical composition (e.g., Stakes et al., 1991; Vanko and Stakes, 1991; Gillis, 1996; Tribuzio et al., 2000). This is partly because amphibole formed at higher temperatures is easily overprinted or replaced by later-stage amphibole formed at lower temperatures. Thus, the overlapping by multiple generations of amphibole makes it difficult to discuss the origin of amphibole. As a result, it may not be meaningful to try to specify the origin of the individual amphibole grains.

Overall, although the metamorphic and hydrothermal processes that have occurred under relatively low temperature conditions have been described in detail for oceanic gabbros, those of the incipient stage under rather high temperature conditions have not been fully described, partly because of the difficulties due to overprint by later, lower-temperature products, as mentioned above. So we tried to focus on the transition from the latest stage of magmatism to the incipient stage of metamorphism recorded in the gabbroic rocks of Hole 735B. As a result, we found a new type of veins, the "high-temperature microscopic veins," from olivine gabbros. Information from the veins and related textures can reduce the difficulty in "amphibole-alone mineralogy" mentioned above and yields some constraints on fluid migration under high-temperature conditions in lower crustal olivine gabbros beneath slow-spreading ridges.

ANALYTICAL METHODS

We examined 202 thin sections from 199 specimens sampled by J. Maeda and E. Kikawa during Leg 176. These thin sections contain 217 lithologies (Table T1). Ordinary petrographic descriptions were done under the microscope, with special attention to veins composed of high-temperature minerals. Observations made on enlarged photos taken with Minolta F-3000, a film scanner that has an attachment designed for a thin section, were very useful for identification of the veins described here. Microprobe analyses were done at the State University of New York at Binghamton with a JEOL-8900 during the stay of J. Maeda. Microprobe operations and data correction procedures are the same as in Naslund (1995).

T1. High-temperature microscopic veins, p. 43.

DESCRIPTION OF THE HIGH-TEMPERATURE MICROSCOPIC VEINS AND RELATED TEXTURES

During petrographic observations, we found a type of microscopic vein in 31 (~14%) of 217 lithologies in 199 samples (Tables T1, T2). Samples containing the veins are olivine gabbros and gabbros, troctolites, and oxide-rich gabbros, and we did not find the veins in any microgabbros or felsic rocks. However, it is noted that we examined very few microgabbros and felsic rocks.

Because the veins are composed of high-temperature minerals (i.e., clinopyroxene, orthopyroxene, brown amphibole, and plagioclase), for convenience, these veins are called the "high-temperature microscopic veins" in this paper. Figure F1 shows the downhole distribution of the high-temperature microscopic veins. Within the interval of 500–1500 mbsf drilled during Leg 176, the veins are relatively rich at 620–680 and 950–1070 mbsf. We selected four thin sections of olivine gabbro for detailed examination; that is, Samples 176-735B-101R-1 (Piece 7, 106–108 cm [586.16 mbsf]), 176-735B-112R-2 (Piece 1, 64–66 cm [644.62 mbsf]), 176-735B-130R-3 (Piece 11, 93–95 cm [797.57 mbsf]), and 176-735B-156R-3 (Piece 5, 51–54 cm [1027.59 mbsf]). In the next section, we describe the petrography of the examined samples. Petrographic summaries and representative microprobe analyses of the constituent minerals are given in Table T3 and Tables T4, T5, T6, T7, and T8, respectively.

Petrographic Description of the Examined Olivine Gabbros

The olivine gabbros we examined are similar to each other in petrography. These olivine gabbros show coarse- to medium-grained, equigranular to seriate textures and contain olivine, plagioclase, and clinopyroxene as the predominant phases (Fig. F2). There is almost no evidence of ductile and/or brittle deformation, except for the weak undulatory extinction and curvature of twinning of plagioclase. Olivine and plagioclase grains have subhedral to euhedral granular shapes. Olivine is very homogeneous in composition within a single grain and also within a single thin section. The average composition of olivine within the examined thin section ranges from $Fo_{70.3}$ to $Fo_{63.6}$ (Table T3). Thus, the examined olivine gabbros are not primitive in chemistry. The composition of plagioclase is very diverse even in a single thin section due to magmatic zoning in cumulus grains and the presence of less calcic plagioclase in the veins, which are targets of this paper. The compositional range of magmatic plagioclase within a single thin section is from $An_{59.7}$–$An_{47.9}$ to $An_{53.3}$–$An_{45.6}$ (Table T3). Clinopyroxene grains are subhedral to anhedral with granular to ophitic–poikilitic texture. Clinopyroxene compositions are also diverse and heterogeneous within a single thin section because of their complex magmatic and postmagmatic histories. The average Mg# of magmatic clinopyroxenes in the examined samples is from 81.1 to 74.7 (Table T3). Orthopyroxene occurs as thin rims around olivine, and brown amphibole occurs as rims around clinopyroxene and also around Fe-Ti oxides with irregular shapes. These phases are thought to be magmatic products, based on these textures. Orthopyroxene and brown amphibole are also present as small blebs within grains of clinopyroxene. Small amounts of Fe-Ti oxides, sulfides, and apatite are present as accessory minerals. In some samples, brownish green, greenish, and colorless amphiboles occur as

T2. Samples with high-temperature microscopic veins, p. 44.

T3. Mineral chemistry of gabbroic rocks, p. 45.

T4. Microprobe analyses of plagioclase, p. 46.

T5. Microprobe analyses of olivine, p. 48.

T6. Microprobe analyses of clinopyroxene, p. 49.

T7. Microprobe analyses of orthopyroxene, p. 51.

T8. Microprobe analyses of amphibole, p. 53.

F2. Photomicrographs of the examined olivine gabbros, p. 23.

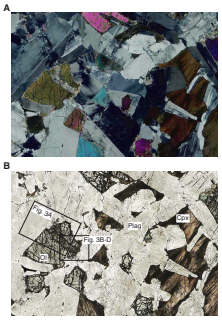

replacement products of clinopyroxene and brown amphibole and also are filling brittle fractures as thin veins within primary phases. These grains of amphibole are clearly metamorphic products based on these textures. The compositions of amphibole are very diverse, as is expected from the variations in texture and color. Chemical features of clinopyroxene, orthopyroxene, and amphibole will be discussed in a later section.

Occurrence of the High-Temperature Microscopic Veins

Figure F3A shows a high-temperature microscopic vein from olivine gabbro (Sample 176-735B-101R-1 [Piece 7, 106–108 cm]) (see Fig. F2A, F2B). In the cumulus grain of olivine ($Fo_{70.3}$), the vein is composed of an aggregate of orthopyroxene (Mg# = 74.9) + brown amphibole + plagioclase. A very narrow magmatic rim of orthopyroxene (inner side) and brown amphibole (outer side) surrounds the cumulus olivine grains. The vein extends into nearby magmatic plagioclase (~An_{60}–An_{48}), where it is composed of less calcic plagioclase (~An_{42}–An_{25}). The distinction between the magmatic plagioclase and the vein plagioclase under the microscope is easy because of the difference in birefringence (Fig. F3A). A compositional map clearly shows a difference between the magmatic plagioclase and vein plagioclase (Fig. F3B, F3C, F3D). The boundaries between the two stages of plagioclase are diffuse and very irregular. In general, the widths of these veins are thicker in magmatic plagioclase than in mafic silicates and are not constant in magmatic plagioclase, that is, they irregularly expand and contract (Fig. F3A). In this case, the width of the vein is ~400–800 µm at most. Figure F4 shows the histogram of An% of the analyzed plagioclase in this area of the thin section, clearly indicating a bimodal distribution of calcic plagioclase of magmatic origin and less calcic plagioclase in the veins, although this does not indicate the true proportions of these two stages of plagioclase. It is noteworthy, however, that the vein plagioclase is not always less calcic. Some parts of the veins, especially within the olivine grains, contain plagioclase as calcic as the magmatic plagioclase (up to $An_{57.5}$ in this case) (Figs. F3B, F3C, F3D, F4). Therefore, it is likely that during the formation of the veins (at least in the earlier stage), physicochemical conditions were not very different from those for the magmatic plagioclase. This may be also suggested by the same mineralogy in the magmatic rims on olivine and in the veins (i.e., orthopyroxene and brown amphibole).

In Figure F5 (Sample 176-735B-130R-3 [Piece 11, 93–95 cm]), two high-temperature microscopic veins are cutting magmatic grains of olivine, clinopyroxene, and plagioclase. In this case, the width of the vein is ~80–200 µm at most. The petrographic features of these veins within the grains of olivine and plagioclase are very similar to those in Figure F3. In the magmatic plagioclase ($An_{53.3}$–$An_{52.0}$), the boundary between the magmatic plagioclase and less-calcic plagioclase ($An_{48.7}$–$An_{37.3}$) of the vein is diffuse and irregular. The extension of this vein into the magmatic clinopyroxene is marked by a discontinuous, irregular alignment of elongated blebs composed of brown amphibole (±plagioclase). This discontinuous and irregular occurrence is very peculiar by contrast with the microgabbro veins and lower-temperature hydrothermal veins reported from Hole 735B cores. The latter veins have straight and sharp contacts against the host minerals and a nearly constant width in mi-

F3. Occurrence of the high-temperature microscopic veins, p. 25.

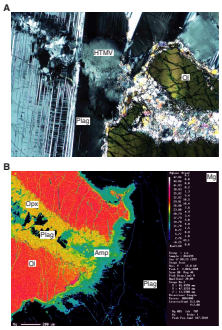

F4. Histogram showing An% of plagioclase, p. 27.

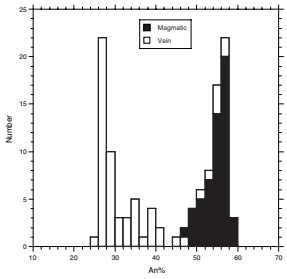

F5. Occurrence of the high-temperature microscopic veins, p. 28.

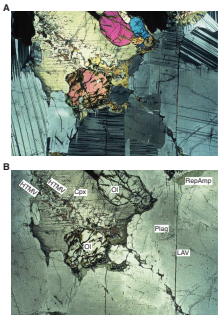

croscopic or macroscopic scale, in general. In this thin section, the high-temperature microscopic vein is furthermore cut by a later, lower-temperature vein of brownish green to green amphibole, which looks like fillings within brittle fractures of the plagioclase grains. Similar greenish amphiboles are also observed within the high-temperature veins as discontinuous alignments with very irregular shapes and are also filling brittle fractures in the magmatic plagioclase. These observations suggest that this high-temperature microscopic vein survived during the rather long transition from higher- to lower-temperature conditions or was reactivated at lower-temperature conditions. Based on this occurrence, these brownish green to green amphiboles are referred to as "later amphiboles" in this paper.

Figure F6A and F6B shows a photomicrograph of olivine gabbro (Sample 176-735B-156R-3 [Piece 5, 51–54 cm]) (see Fig. F2C, F2D). A subhedral to anhedral grain of clinopyroxene (Mg# = 80.7–70.7) is penetrated by a high-temperature microscopic vein. This vein is composed of plagioclase ($An_{35.3}$–$An_{30.3}$) and brown amphibole within the grain of clinopyroxene and can be traced into the nearby magmatic plagioclase chadacryst ($An_{54.7}$–$An_{52.7}$) enclosed in the clinopyroxene grain. In this case, the width of the vein is ~100–300 µm at most. The mode of occurrence and compositional features of magmatic and vein plagioclase are the same as shown in Figure F3A. It is noteworthy in this figure that vermicular intergrowths of brown amphibole + orthopyroxene (Mg# = 71.8–68.4) occurred in clinopyroxene on both sides of the vein. This very symmetrical occurrence of the intergrowth relative to the high-temperature microscopic vein strongly suggests that the origin of the intergrowth is related to the penetration of the vein. The chemical compositions of the clinopyroxene are different in the parts with and without the intergrowth (Fig. F6C, F6D). This difference can be related to the penetration of the vein and formation of the intergrowth.

One of the most important features of these high-temperature microscopic veins is the mineral assemblage. Most veins are composed of clinopyroxene, orthopyroxene, brown amphibole, and plagioclase and virtually do not contain lower-temperature minerals, such as chlorite, smectite, epidote, prehnite, and/or talc, for example. Although some veins contain these low-temperature products (e.g., the later amphiboles mentioned above), these phases overprinted the earlier, higher-temperature phases. Another important feature is a dependence of mineralogy on the host magmatic minerals; that is, the mineral assemblages of the veins are strongly controlled by the host magmatic minerals penetrated by the veins. The "along-vein variation" in mineralogy of veins has also been described from the gabbros of Hole 735B (e.g., Mével and Cannat, 1991) and from the Mid-Atlantic Ridge at the Kane Fracture Zone (MARK) area (Gillis et al., 1993), but in veins that consist of lower-temperature minerals and are completely different from those described here. The significance of the along-vein variations will be discussed in a later section.

Interfingering Textures of Clinopyroxene with Intergrowths of Amphibole + Orthopyroxene

In the previous section, the intergrowth of brown amphibole + orthopyroxene in clinopyroxene grains along the high-temperature microscopic veins was described (Fig. F6). The very symmetrical occurrence of the intergrowth to the high-temperature microscopic vein

F6. Occurrence of the high-temperature microscopic vein with intergrowths, p. 29.

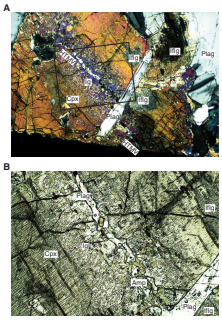

strongly suggests that these two features are genetically linked to each other. In this section we describe another occurrence of brown amphibole + orthopyroxene intergrowth in clinopyroxene.

Figure F7A and F7B shows grains of clinopyroxene ~2 cm away from the clinopyroxene grain shown in Figure F6 (see Fig. F2C, F2D). Contacts between the two grains of clinopyroxene are interpenetrating and interlocking to each other. We tentatively call this texture an "interfingering" texture. This is a very common texture in olivine gabbros recovered from Hole 735B, and we observed this texture in ~62% of the examined samples (see Table T9; Fig. F1). In some cases, dependent on the cutting direction of thin sections, a grain of interfingering clinopyroxene looks like an inclusion within another grain of clinopyroxene (Fig. F6A).

An important feature of this texture is the occurrence of intergrowths of brown amphibole + orthopyroxene in these interfingering areas. Figure F7C and F7D show compositional maps for nearly the same area (see Fig. F2C, F2D). The interfingering area of clinopyroxene grains contains blebs of orthopyroxene and brown amphibole. Whereas, in general, grains of magmatic clinopyroxene in olivine gabbros are slightly dark under the microscope due to the presence of many thin exsolution lamellae of Fe-Ti oxide, within the interfingering area such lamellae are scarce and the development of (100) cleavage is also very weak. As a result, the interfingering parts of clinopyroxene look very clear under the microscope. These same features of clinopyroxene are also observed in clinopyroxene with intergrowths near the high-temperature microscopic veins (Fig. F5A, F5B) and are also common in secondary clinopyroxenes observed in oceanic gabbros (e.g., Ito and Anderson, 1983; Mével, 1987, 1988; Gillis et al., 1993; Gillis, 1995, 1996; Manning and MacLeod, 1996). Overall, it is noteworthy that two kinds of brown amphibole + orthopyroxene intergrowth are very similar in petrography and are not distinguished from each other.

F7. Occurrence of the interfingering texture of clinopyroxene in olivine gabbro, p. 31.

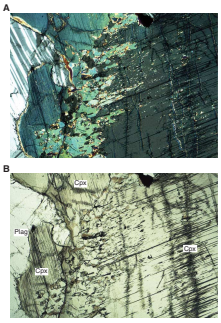

T9. Interfingering texture of clinopyroxene, p. 55.

CHEMICAL COMPOSITIONS OF CLINOPYROXENE, ORTHOPYROXENE, AND AMPHIBOLE FROM THE HIGH-TEMPERATURE MICROSCOPIC VEINS AND THE RELATED TEXTURES

In this section, we compare the chemical compositions of mafic silicates (clinopyroxene, orthopyroxene, and amphibole) from the high-temperature microscopic veins and the related textures. Representative microprobe analyses are given in Tables T4, T5, T6, T7, and T8.

Clinopyroxene

Chemical compositions of clinopyroxene are plotted in Figures F8 and F9. Clinopyroxenes with intergrowths both close to the high-temperature microscopic veins and in the interfingering textures are higher in Wo content (Ca/[Ca+Mg+Fe]) than magmatic clinopyroxenes. This suggests that the former clinopyroxenes, hereafter referred to collectively as secondary clinopyroxenes, were formed under lower-temperature conditions than the latter clinopyroxenes (Fig. F8). The difference in Wo content between magmatic clinopyroxene and secondary clinopyroxene is rather gradational, suggesting that the conditions are also gradational. This is also indicated by the calculated temperatures

F8. Pyroxene quadrilateral, p. 33.

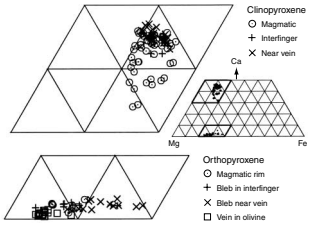

F9. Composition of clinopyroxene, p. 34.

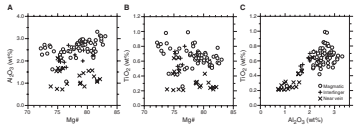

discussed in a later section. The secondary clinopyroxenes near the high-temperature microscopic veins are also clearly lower in Al_2O_3 content than magmatic clinopyroxenes, although the difference is rather gradational. The secondary clinopyroxenes with interfingering textures plot between the magmatic clinopyroxenes and the clinopyroxenes near the high-temperature microscopic veins. TiO_2 contents show a similar tendency to that of Al_2O_3 contents. TiO_2 contents of the interfingering clinopyroxenes are nearly the same or slightly lower than those of the magmatic clinopyroxenes. Clinopyroxenes hosting the intergrowths of brown amphibole + orthopyroxene near the high-temperature microscopic veins are clearly lower in TiO_2 than those of magmatic clinopyroxenes. Magmatic clinopyroxene has exsolution lamellae of Fe-Ti oxide, and therefore the primary TiO_2 content would have been even higher. On the other hand, as mentioned earlier, the secondary clinopyroxenes lack these lamellae and look clear under the microscope, indicating that their lower Ti contents are not due to the exsolution of Fe-Ti oxide. These features of the secondary clinopyroxenes, lower in Ti and Al contents than magmatic clinopyroxenes (Fig. F9C), may be related to the formation of brown, Ti-rich pargasitic amphibole blebs. These chemical and textural features are also common in secondary clinopyroxenes from other oceanic gabbros (e.g., Mével, 1987; Manning and MacLeod, 1996). So the decreases in Al and Ti of secondary clinopyroxene are a very common phenomena in the oceanic crust. Al- and Ti-poor secondary clinopyroxenes are also reported from the Skaergaard layered intrusion (Manning and Bird, 1986) and are interpreted as reflecting exchange with hydrothermal fluids (Manning and MacLeod, 1996).

Orthopyroxene

Orthopyroxene is a subordinate mineral in the olivine gabbros, occurring as magmatic rims on cumulus grains of olivine and as blebs in intergrowths with brown amphibole in clinopyroxene grains both near the high-temperature microscopic veins and within the interfingering textures. Based on textures, orthopyroxene can be divided into four categories: magmatic rims, blebs in the interfingering clinopyroxene, blebs near the high-temperature microscopic veins, and filling high-temperature microscopic veins penetrating olivine grains. There is no detectable difference in composition among these orthopyroxenes (Fig. F8), except for the orthopyroxene filling high-temperature microscopic veins in olivine grains, which are characterized by lower contents of CaO, TiO_2, and Al_2O_3 than those of other orthopyroxenes (Fig. F10). It is likely that these compositional features are attributed to the Ca-, Ti-, and Al-poor nature of olivine, which is a precursor of the orthopyroxene.

Amphibole

Microprobe analyses of amphibole are shown in Figure F11. The procedures for the calculation of amphibole formula used are given in the "Appendix," p. 20. Terminology of amphibole is after Leake et al. (1997). In Figure F11, we classify amphiboles into five categories (i.e., those of magmatic rims, blebs in the interfingering clinopyroxene, blebs near the high-temperature microscopic veins, amphiboles from the high-temperature microscopic veins within olivine grains, and am-

F10. Composition of orthopyroxene, p. 35.

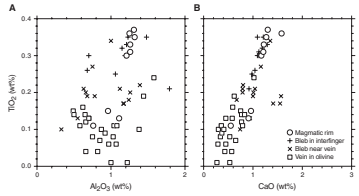

F11. Composition of amphiboles, p. 36.

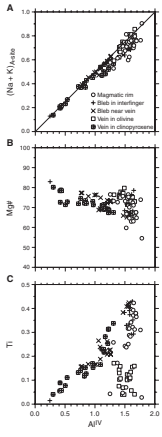

phiboles within clinopyroxene grains). It is noted that, of course, these categories do not include all varieties of amphibole from Hole 735B cores, such as the later amphiboles mentioned above.

In a $(Na + K)_{A\text{-site}}$ vs. Al^{IV} diagram, most of the analyses are plotted on the join between pargasite and tremolite (Fig. F11A). Thus, amphiboles rich in $(Na + K)_{A\text{-site}}$ (≥0.5) are rich in Al^{IV} (≥1.0) and vice versa. In a plot of Mg# vs. Al^{IV} (Fig. F11B), amphiboles from the high-temperature microscopic veins in clinopyroxene grains are slightly lower in Mg# at a given Al^{IV} than other amphiboles. Magmatic amphiboles are pargasite to edenite. Amphibole blebs in clinopyroxene from the interfingering areas are plotted in the field of pargasite, and those near the high-temperature microscopic veins are in the fields of pargasite, edenite, and magnesiohornblende. Amphiboles within the high-temperature microscopic veins are plotted in a wider area of pargasite, edenite, magnesiohornblende, and actinolite. These wider compositional ranges may be partly attributed to overprinting and modification at lower-temperature conditions.

It is noteworthy that amphiboles in the high-temperature microscopic veins penetrating olivine grains are characteristically low in Ti (or high in Al^{IV} and lower in Si) compared to those formed in clinopyroxene grains (Fig. F11C). This may be attributed to Ti-poor (or Si-poor) nature of olivine, precursor of these amphiboles. Similar observations are also reported from the Hess Deep gabbros (e.g., Manning and MacLeod, 1996).

TEMPERATURE CONDITIONS OF THE HIGH-TEMPERATURE MICROSCOPIC VEINS AND INTERGROWTHS

Crystallization temperatures have been calculated to evaluate the conditions of formation of the high-temperature microscopic veins and the intergrowths of brown amphibole + orthopyroxene as well as those of magmatic phases. Since the compositions of the minerals may have been changed during later-stage, lower-temperature processes, the calculated temperatures may be minimum values. Clinopyroxene and orthopyroxene temperatures were calculated with the geothermometer proposed by Lindsley and Anderson (1983) using the program written by Anderson et al. (1993), and amphibole–plagioclase temperatures were calculated with the geothermometer proposed by Holland and Blundy (1994). These calculations were made by assuming a pressure of 2 kbar, but the results are not particularly pressure sensitive. The calculated temperatures are shown in Table T10 and Figure F12.

Calculated temperatures for clinopyroxenes hosting the intergrowths near the high-temperature microscopic veins (1000°–700°C) and within the interfingering parts (1000°–840°C) are lower than those of magmatic clinopyroxenes (1200°–800°C). Temperatures of orthopyroxene blebs near the veins and in the interfingering clinopyroxenes are 1020°–820°C and are similar to those of the clinopyroxene hosting these orthopyroxene blebs. Amphibole–plagioclase temperatures for the high-temperature microscopic veins are 820°–650°C. Overall, the temperature data indicate that the interfingering textures and the high-temperature microscopic veins were formed under similar and rather high-temperature conditions up to 1000°C. One of the most important results of the temperature calculation is that the temperatures are gra-

T10. Calculated temperatures, p. 56.

F12. Temperatures calculated for clinopyroxene, orthopyroxene, and amphibole-plagioclase, p. 38.

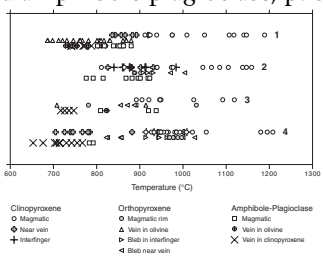

dational from the magmatic stage to the stage of the high-temperature microscopic vein and interfingering textures without a significant break (Fig. F12). This suggests that the penetration of the high-temperature microscopic veins and the formation of the intergrowth textures followed just after (or were coeval with the latest stage of) the magma crystallization.

DISCUSSION

Relation between the High-Temperature Microscopic Veins and the Interfingering Texture of Clinopyroxene

Before the discussion on the origin of the high-temperature microscopic veins, we need to pay attention to the relation between the veins and the interfingering texture of clinopyroxene. As already mentioned, these two features contain the intergrowth of brown amphibole + orthopyroxene in clinopyroxene grains. These two kinds of the intergrowths are essentially similar to each other in texture (Figs. F6, F7) in chemical compositions of the involved minerals (Figs. F8, F9, F10, F11) and in the calculated temperatures (Fig. F12). These observations suggest that both intergrowth textures, and therefore both the high-temperature microscopic vein and the interfingering clinopyroxene, were formed under nearly the same conditions at the same time. We propose here that the interfingering texture of clinopyroxene and the high-temperature microscopic veins were formed through a common process. This is supported by an intimate association of these two features observed in several thin sections (Figs. F6A, F13A, F13C).

F13. Photomicrographs of olivine gabbros, p. 39.

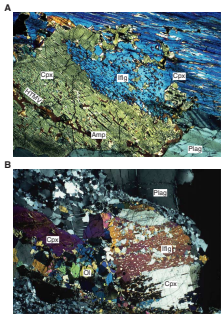

Origin of the High-Temperature Microscopic Veins: Fluid Origin or Silicate Melt Origin?

There are two candidates for the origin of the high-temperature microscopic vein, namely silicate melt origin or fluid origin. Although we have no direct evidence such as geochemical data from the veins, we can discuss it based on the occurrences of the veins themselves. The discontinuous and irregular occurrence (Fig. F5) and the along-vein variation in mineralogy suggest that these veins were formed by reaction of magmatic minerals with some kind of fluids under the conditions of low fluid/rock ratios. This is supported by the composition of the minerals in the veins. Al- and Ti-poor features of the secondary clinopyroxene (Fig. F9) compared to primary clinopyroxene are also reported from the Skaergaard intrusion as product of exchange between primary minerals and fluid (Manning and MacLeod, 1996). Orthopyroxenes and brown amphiboles from the veins within olivine grains are characterized by lower Ti, Ca, and Al contents and Ti content, respectively, compared to these minerals within clinopyroxene grains (Figs. F10, F11). Thus, the vein-constituting, secondary minerals inherited the chemical signatures from the primary, precursory phases, which suggests a reaction between the primary phases and migrating fluids.

Based on petrographical observations, the reactions between magmatic minerals and migrating fluids can be written as follows:

$$\text{Olivine} + \text{fluid}_1 = \text{orthopyroxene} + \text{brown amphibole} + \text{plagioclase} + \text{fluid}_2 \text{ (in olivine)},$$

Plagioclase + $fluid_3$ = less calcic plagioclase + $fluid_4$ (in plagioclase),

Clinopyroxene + $fluid_5$ = brown amphibole + plagioclase + $fluid_6$ (in clinopyroxene), and

Clinopyroxene + $fluid_7$ = orthopyroxene + brown amphibole + Ti- and Al-poor clinopyroxene + $fluid_8$ (for the intergrowths near the high-temperature microscopic veins and the interfingering clinopyroxene).

We cannot quantitatively determine these reaction equations because of the heterogeneity in mineral composition and the lack of accurate data on volumes of the involved phases and the actual volume changes in the examined samples. In any case, addition and/or subtraction of components by fluid migrations are required for all the above equations, although the compositions of the fluids are not elucidated in this study.

Origin of the Fluid: Magmatic Origin or Seawater Origin?

There are also, in this case, two candidates for the origin of the fluid phase, that is, magmatic fluid and hydrothermal fluid originated from seawater. Although it is very difficult to get unequivocal answer at present, we would like to try to discuss the origin of the fluid phase based on available information.

In general, it is accepted that the penetration of seawater does not predate ductile deformation due to lithospheric stretching within Layer 3 gabbros of slow-spreading ridges (Mével and Cannat, 1991). Therefore, the origin of the fluid phase cannot be attributed to the penetration of seawater, if there is evidence suggesting that the timing of the veins predated ductile deformation. As shown in the previous section (Figs. **F3, F5**), olivine, plagioclase and clinopyroxene were dissolved by the penetration of these veins and there is no mechanical offset along the high-temperature microscopic veins. This indicates that the penetration of the veins did not accompany the deformation and also did not take place through brittle fracture networks. Figure **F13B** shows the interfingering texture in deformed olivine gabbro (Sample 176-735B-148R-1 [Piece 2, 104–112 cm]). In this sample, the interfingering texture is clearly involved in the ductile deformation. This indicates that the formation of the interfingering texture predated ductile deformation. Furthermore there is evidence suggesting that the formation of the veins preceded the complete solidification of the gabbroic crystal mush. Most of the high-temperature microscopic veins clearly penetrate not only cumulus phases but subhedral to anhedral intercumulus phases as well (Figs. **F3, F5, F6**). However, some high-temperature microscopic veins occur along grain boundaries of magmatic minerals (Fig. **F13C**) (Sample 176-735B-101R-1 [Piece 7, 106–108 cm]). In this case, the high-temperature microscopic vein is running in the outer edge of a plagioclase grain, and a very fine-grained intergrowth of orthopyroxene + brown amphibole was formed in the edge of a clinopyroxene in contact with a high-temperature microscopic vein. These textures suggest that the timing of the penetration of the high-temperature microscopic veins might be before complete solidification of the gabbroic crystal mush. The boundary of the cumulus phases ap-

pears to have been still wet with trapped evolved melt, so that it was easier to move along the boundaries of magmatic phases. These lines of petrographic evidence suggest that the penetration of the high-temperature microscopic veins did not take place in completely solidified gabbros. Therefore, it is concluded that the penetration of the high-temperature microscopic veins predated ductile deformation. This conclusion indicates that the high-temperature microscopic veins cannot be related to the seawater migration. So by elimination, our preliminary conclusion is that the fluid phase responsible for the high-temperature microscopic veins and interfingering clinopyroxenes is of magmatic origin, although >90% crystallization of mid-ocean-ridge basalt (MORB) magma is necessary for the saturation and exsolution of fluid phase because of the nearly anhydrous nature of MORB (e.g., Nehlig, 1993; Dixon and Stolper, 1995; Dixon et al., 1995). This preliminary explanation is dependent on the hypothesis that the penetration of seawater does not predate ductile deformation within Layer 3 gabbros of slow-spreading ridges; therefore, we need additional data directly implying magmatic origin, such as isotopic and trace element data.

Kelley and Delaney (1986) and Kelley et al. (1993) mentioned, based on fluid inclusion data, that the exsolution of fluid from the latest-stage magma took place at a temperature >700°C in the MARK area. However, no obvious mineralogical expression for these magmatic fluids has been found until now. A plausible candidate for the mineralogical expression of the magmatic fluid is brown amphibole, which is observed within a corona of olivine (Kelley et al., 1993, for the MARK gabbros). Tribuzio et al. (2000) discussed the origin of interstitial brown amphibole from gabbros in the North Apennine ophiolites, which are considered to be formed at a slow-spreading ridge. They proposed that the brown amphibole might be a product of an interaction between infiltrating exsolved magmatic fluid and gabbroic crystal mush. We now propose an alternative explanation that the high-temperature microscopic veins we found are a mineralogical manifestation of the migration of fluids derived from late-stage magma beneath spreading ridges.

Because there is no axial fault and high-temperature ductile shear zone in the deep crust at fast-spreading ridges, it is difficult to assume seawater penetration at higher-temperature conditions. So it is proposed that the onset of metamorphism and hydrothermal penetration occurs at ~500°C and is triggered by downward propagation of a cracking front (Mével and Cannat, 1991). However, hydration at temperatures of ~800°–600°C is reported from the Hess Deep gabbros (e.g., Gillis. 1995; Manning and MacLeod, 1996; Manning et al., 1996). To the proposal by Manning and MacLeod (1996) that localized brittle deformation near the magma body under higher-temperature conditions promoted seawater–rock interaction, we can add another explanation that high-temperature hydration occurs by migration of fluid phases from evolved magmas at fast-spreading ridges without any incorporation of seawater. The exsolution of fluids from evolved magmas should not be restricted to slow-spreading environments, and therefore the veins described here should also be found at fast-spreading ridges.

CONCLUSIONS

1. A type of microscopic vein is found in olivine gabbros recovered from Ocean Drilling Program Hole 735B on the Southwest Indian Ridge during Leg 176. These veins are composed of high-

temperature minerals (i.e., clinopyroxene, orthopyroxene, brown amphibole, and plagioclase) and yield important information about the magmatic/hydrothermal transition beneath the Southwest Indian Ridge.

2. An important feature of these veins is the along-vein variation in mineralogy, which is strongly correlated with the primary magmatic phase, in which the veins penetrate. Within grains of magmatic plagioclase, the veins are composed of less calcic plagioclase. In grains of olivine, the veins are composed of orthopyroxene + brown amphibole + plagioclase. In clinopyroxene grains, the veins consist of plagioclase and brown amphibole and are accompanied by intergrowths of brown amphibole + orthopyroxene. The occurrence of the intergrowths is completely symmetrical relative to the veins, indicating an intimate genetic relationship between the intergrowth and the microscopic vein. Very similar intergrowths are observed in clinopyroxene grains with the interfingering textures. Similarity between the petrographical features and the chemical compositions of the minerals in the two kinds of intergrowths indicates that they were formed under essentially the same conditions and by the same process.
3. Although calculated temperatures of the minerals from the veins and nearby intergrowths (up to 1000°C) are lower than those of magmatic clinopyroxenes (1200°–800°C), the difference is gradational without any substantial gap between them. This suggests that the formation of the veins and the interfingering textures occurred during the latest stage of (or just after) magmatic crystallization of olivine gabbros. Petrographic evidence also suggests that the penetration of the veins and the formation of the interfingering texture predated complete solidification of the gabbroic crystal mush as well as the ductile deformation.
4. Although the veins are composed of silicate minerals, the discontinuous and irregular occurrence and the along-vein variation of the veins cannot be explained if these veins were crystallized from silicate melts. Consequently, these veins and nearby intergrowths are most likely to be formed by the reaction of magmatic minerals with fluids under the condition of low fluid/rock ratios.
5. In general, it is accepted that the penetration of seawater into Layer 3 gabbros does not predate ductile deformation due to lithospheric stretching beneath slow-spreading ridges (Mével and Cannat, 1991). Therefore, the origin of the fluid phase that appears to predate ductile deformation cannot be attributed to the penetration of seawater. It is likely that the fluids originated from evolved magma by exsolution. We propose that the microscopic veins yield mineralogical evidence for the exsolution and percolation of high-temperature fluid derived from latest-stage magma beneath the Southwest Indian Ridge.
6. The exsolution of magmatic fluids at high-temperature conditions is not restricted to slow-spreading environments. The discrepancy between the hydration temperatures of ~800°–600°C observed for the gabbros from fast-spreading ridges, and 500°C assumed for the penetration of seawater at fast-spreading ridges by a simple cracking front model, can be explained, if the exsolution of magmatic fluids occurred at the higher temperatures.

ACKNOWLEDGMENTS

We would like to thank the scientists, as well as the captain, the crew, and the staff of the *JOIDES Resolution* for their support and cooperation during Leg 176. We thank K.M. Gillis, M.J. Toplis, H.J.B. Dick, and D.J. Miller for insightful reviews of the manuscript. We also thank Shiro Hasegawa, Tadao Hirama, Yuko Suzuki, and Ayako Kurokawa for help during the research and preparation of the manuscript. Most of this research was done at the State University of New York at Binghamton during the stay of J. Maeda from October 1998 to August 1999.

This research used samples and/or data provided by the Ocean Drilling Program (ODP). ODP is sponsored by the U.S. National Science Foundation (NSF) and participating countries under management of Joint Oceanographic Institutions (JOI), Inc. Funding for this research was provided to J. Maeda by the Ministry of Education, Science, and Culture of Japan. H.R. Naslund was supported by USSAC postcruise funds.

REFERENCES

Anderson, D.J., Lindsley, D.H., and Davidson, P.M., 1993. QUILF: a PASCAL program to assess equilibria among Fe-Mg-Ti oxides, pyroxenes, olivine and quartz. *Comput. Geosci.,* 19:1333–1350.

Cannat, M., 1991. Plastic deformation at an oceanic spreading ridge: a microstructural study of Site 735 gabbros (southwest Indian Ocean). *In* Von Herzen, R.P., Robinson, P.T., et al., *Proc. ODP, Sci. Results,* 118: College Station, TX (Ocean Drilling Program), 399–408.

Cannat, M., Mével, C., and Stakes, D.S., 1991. Stretching of the deep crust at the slow spreading SW Indian Ridge. *Tectonophysics,* 190:73–95.

Cosca, M.A., Essene, E.J., and Bowman, J.R., 1991. Complete chemical analyses of metamorphic hornblendes: implications for normalization, calculated H_2O activities, and thermobarometry. *Contrib. Mineral. Petrol.,* 108:472–484.

Dick, H.J.B., Meyer, P.S., Bloomer, S., Kirby, S., Stakes, D., and Mawer, C., 1991a. Lithostratigraphic evolution of an in-situ section of oceanic Layer 3. *In* Von Herzen, R.P., Robinson, P.T., et al., *Proc. ODP, Sci. Results,* 118: College Station, TX (Ocean Drilling Program), 439–538.

Dick, H.J.B., Natland, J.H., Alt, J.C., Bach, W., Bideau, D., Gee, J.S., Haggas, S., Hertogen, J.G.H., Hirth, G., Holm, P.M., Ildefonse, B., Iturrino, G.J., John, B.E., Kelley, D.S., Kikawa, E., Kingdon, A., LeRoux, P.J., Maeda, J., Meyer, P.S., Miller, D.J., Naslund, H.R., Niu, Y., Robinson, P.T., Snow, J., Stephen, R.A., Trimby, P.W., Worm, H.-U., and Yoshinobu, A., 2000. A long in situ section of the lower ocean crust: results of ODP Leg 176 drilling at the Southwest Indian Ridge. *Earth Planet. Sci. Lett.,* 179:31–51.

Dick, H.J.B., Natland, J.H., Miller, D.J., et al., 1999. *Proc. ODP, Init. Repts.,* 176 [CD-ROM]. Available from: Ocean Drilling Program, Texas A&M University, College Station, TX 77845-9547, U.S.A.

Dick, H.J.B., Schouten, H., Meyer, P.S., Gallo, D.G., Bergh, H., Tyce, R., Patriat, P., Johnson, K.T.M., Snow, J., and Fisher, A., 1991b. Tectonic evolution of the Atlantis II Fracture Zone. *In* Von Herzen, R.P., Robinson, P.T., et al., *Proc. ODP, Sci. Results,* 118: College Station, TX (Ocean Drilling Program), 359–398.

Dixon, J.E., and Stolper, E.M., 1995. An experimental study of water and carbon dioxide solubilities in mid-ocean ridge basaltic liquids. Part II: Applications to degassing. *J. Petrol.,* 36:1633–1646.

Dixon, J.E., Stolper, E.M., and Holloway, J.R., 1995. An experimental study of water and carbon dioxide solubilities in mid-ocean ridge basaltic liquids. Part I: Calibration and solubility models. *J. Petrol.,* 36:1607–1631.

Fisher, R.L., and Sclater, J.G., 1983. Tectonic evolution of the southwest Indian Ocean since the mid-Cretaceous: plate motions and stability of the pole of Antarctica/Africa for at least 80 Myr. *Geophys. J. R. Astron. Soc.,* 73:553–576.

Gillis, K.M., 1995. Controls on hydrothermal alteration in a section of fast spreading oceanic crust. *Earth Planet. Sci. Lett.,* 134:473–489.

————, 1996. Rare earth element constraints on the origin of amphibole in gabbroic rocks from Site 894, Hess Deep. *In* Mével, C., Gillis, K.M., Allan, J.F., and Meyer, P.S. (Eds.), *Proc. ODP, Sci. Results,* 147: College Station, TX (Ocean Drilling Program), 59–75.

Gillis, K.M., and Roberts, M.D., 1999. Cracking at the magma-hydrothermal transition: evidence from the Troodos ophiolite, Cyprus. *Earth Planet. Sci. Lett.,* 169:227–244.

Gillis, K.M., Thompson, G., and Kelley, D.S., 1993. A view of the lower crustal component of hydrothermal systems at the Mid-Atlantic Ridge. *J. Geophys. Res.,* 98:19597–19619.

Hart, S.R., Blusztajn, J., Dick, H.J.B., Meyer, P.S., and Muehlenbachs, K., 1999. The fingerprint of seawater circulation in a 500-meter section of ocean crust gabbros. *Geochim. Cosmochim. Acta,* 63:4059–4080.

Holland, T., and Blundy, J., 1994. Non-ideal interactions in calcic amphiboles and their bearing on amphibole–plagioclase thermometry. *Contrib. Mineral. Petrol.,* 116:433–447.

Ito, E., and Anderson, A.T., Jr., 1983. Submarine metamorphism of gabbros from the Mid-Cayman Rise: petrographic and mineralogic constraints on hydrothermal processes at slow-spreading ridges. *Contrib. Mineral. Petrol.,* 82:371–388.

Kelley, D.S., 1996. Methane-rich fluids in the oceanic crust. *J. Geophys. Res.,* 101:2943–2962.

————, 1997. Fluid evolution in slow-spreading environments. *In* Karson, J.A., Cannat, M., Miller, D.J., and Elthon, D. (Eds.), *Proc. ODP, Sci. Results,* 153: College Station, TX (Ocean Drilling Program), 399–415.

Kelley, D.S., and Delaney, J.R., 1987. Two-phase separation and fracturing in mid-ocean ridge gabbros at temperatures greater than 700°C. *Earth Planet. Sci. Lett.,* 83:53–66.

Kelley, D.S., and Früh-Green, G.L., 1999. Abiogenic methane in deep-seated mid-ocean ridge environments: insights from stable isotope analyses. *J. Geophys. Res.,* 104:10439–10460.

————, in press. Volatile lines of descent in submarine plutonic environments: insights from stable isotope and fluid inclusion analyses. *Geochim. Cosmochim. Acta.*

Kelley, D.S., Gillis, K.M., and Thompson, G., 1993. Fluid evolution in submarine magma-hydrothermal systems at the Mid-Atlantic Ridge. *J. Geophys. Res.,* 98:19579–19596.

Kempton, P.D., Hawkesworth, C.J., and Fowler, M., 1991. Geochemistry and isotopic composition of gabbros from Layer 3 of the Indian Ocean crust, Hole 735B. *In* Von Herzen, R.P., Robinson, P.T., et al., *Proc. ODP, Sci. Results,* 118: College Station, TX (Ocean Drilling Program), 127–143.

Leake, B.E., Wooley, A.R., Arps, C.E.S., Birch, W.D., Gilbert, M.C., Grice, J.D., Hawthorne, F.C., Kato, A., Kisch, H.J., Krivovichev, V.G., Linthout, K., Laird, J., Mandarino, J., Maresch, W.V., Nickel, E.H., Rock, N.M.S., Schumacher, J.C., Smith, D.C., Stephenson, N.C.N., Ungaretti, L., Whittaker, E.J.W., and Youzhi, G., 1997. Nomenclature of amphiboles: report of the Subcommittee on Amphiboles in the International Mineralogical Association Commission on New Minerals and Mineral Names. *Am. Mineral.,* 82:1019–1037.

Lindsley, D.H., and Andersen, D.J., 1983. A two-pyroxene thermometer. *J. Geophys. Res.,* 88 (Suppl.):A887–A906.

Lister, C.R.B., 1974. On the penetration of water into hot rock. *Geophys. J. R. Astron. Soc.,* 39:465–509.

MacLeod, C.J., Boudier, F., Yaouancq, G., and Richter, C., 1996. Gabbro fabrics from Site 894, Hess Deep: implications for magma chamber processes at the East Pacific Rise. *In* Mével, C., Gillis, K.M., Allan, J.F., and Meyer, P.S. (Eds.), *Proc. ODP, Sci. Results,* 147: College Station, TX (Ocean Drilling Program), 317–328.

Magde, L.S., Dick, H.J.B., and Hart, S.R., 1995. Tectonics, alteration and fractal distribution of hydrothermal veins in the lower ocean crust. *Earth Planet. Sci. Lett.,* 129:103–119.

Manning, C.E., and Bird, D.K., 1986. Hydrothermal clinopyroxenes of the Skaergaard intrusion. *Contrib. Mineral. Petrol.,* 92:437–447.

Manning, C.E., and MacLeod, C.J., 1996. Fracture-controlled metamorphism of Hess Deep gabbros, Site 894: constraints on the roots of mid-ocean-ridge hydrothermal systems at fast-spreading centers. *In* Mével, C., Gillis, K.M., Allan, J.F., and Meyer, P.S. (Eds.), *Proc. ODP, Sci. Results,* 147: College Station, TX (Ocean Drilling Program), 189–212.

Manning, C.E., Weston, P.E., and Mahon, K.I., 1996. Rapid high-temperature metamorphism of East Pacific Rise gabbros from Hess Deep. *Earth Planet. Sci. Lett.,* 144:123–132.

McCollom, T.M., and Shock, E.L., 1998. Fluid-rock interactions in the lower oceanic crust: thermodynamic models of hydrothermal alteration. *J. Geophys. Res.,* 103:547–575.

Mével, C., 1987. Evolution of oceanic gabbros from DSDP Leg 82: influence of the fluid phase on metamorphic crystallizations. *Earth Planet. Sci. Lett.,* 83:67–79.

————, 1988. Metamorphism of oceanic layer 3, Gorringe Bank, eastern Atlantic. *Contrib. Mineral. Petrol.,* 100:496–509.

Mével, C., and Cannat, M., 1991. Lithospheric stretching and hydrothermal processes in oceanic gabbros from slow-spreading ridges. *In* Peters, T., Nicolas, A., and Coleman, R.J. (Eds.), *Ophiolite Genesis and Evolution of the Oceanic Lithosphere:* Dordrecht (Kluwer), 293–312.

Muller, M.R., Robinson, C.J., Minshull, T.A., White, R.S., and Bickle, M.J., 1997. Thin crust beneath Ocean Drilling Program Borehole 735B at the Southwest Indian Ridge? *Earth Planet. Sci. Lett.,* 148:93–107.

Naslund, H.R., 1995. Grain-size, morphological, and compositional variations in igneous silicates in medium-grained diabase from Hole 504B. *In* Erzinger, J., Becker, K., Dick, H.J.B., and Stokking, L.B. (Eds.), *Proc. ODP, Sci. Results,* 137/140: College Station, TX (Ocean Drilling Program), 3–17.

Nehlig, P., 1993. Interactions between magma chambers and hydrothermal systems: oceanic and ophiolitic constraints. *J. Geophys. Res.,* 98:19621–19633.

Pflumio, C., 1991. Evidences for polyphased oceanic alteration of the extrusive sequence of the Semail ophiolite from the Salahi Block (Northern *In* Peters, T., Nicolas, A., and Coleman, R.J. (Eds.), *Ophiolite Genesis and Evolution of the Oceanic Lithosphere:* Dordrecht (Kluwer), 313–351.

Robinson, P., Spear, F.S., Schumacher, J.C., Laird, J., Klein, C., Evans, B.W., and Doolan, B.L., 1982. Phase relations of metamorphic amphiboles: natural occurrence and theory. *In* Veblen, D.R., and Ribbe, P.H. (Eds.), *Amphiboles: Petrology and Experimental Phase Relations*. Rev. Mineral., 9B:1–227.

Robinson, P.T., Dick, H.J.B., and Von Herzen, R.P., 1991. Metamorphism and alteration in oceanic layer 3: Hole 735B. *In* Von Herzen, R.P., Robinson, P.T., et al., *Proc. ODP, Sci. Results,* 118: College Station, TX (Ocean Drilling Program), 541–552.

Robinson, P.T., Von Herzen, R., et al., 1989. *Proc. ODP, Init. Repts.,* 118: College Station, TX (Ocean Drilling Program).

Schiffman, P., Evarts, P., Williams, R.C., and Pickthorn, W.J., 1991. Hydrothermal metamorphism in oceanic crust from the Coast Range ophiolite of California: fluid-rock interaction in a rifted island arc. *In* Peters, T., Nicolas, A., and Coleman, R.J. (Eds), *Ophiolite Genesis and Evolution of the Oceanic Lithosphere:* Dordrecht (Kluwer), 399–426.

Stakes, D., Mével, C., Cannat, M., and Chaput, T., 1991. Metamorphic stratigraphy of Hole 735B. *In* Von Herzen, R.P., Robinson, P.T., et al., *Proc. ODP, Sci. Results,* 118: College Station, TX (Ocean Drilling Program), 153–180.

Talbi, E.H., Honnorez, J., Clauer, N., Gauthier-Lafaye, F., and Stille, P., 1999. Petrology, isotope geochemistry and chemical budgets of oceanic gabbros–seawater interactions in the Equatorial Atlantic. *Contrib. Mineral. Petrol.,* 137:246–266.

Tribuzio, R., Tiepolo, M., and Thirlwall, M.F., 2000. Origin of titanian pargasite in gabbroic rocks from the Northern Apennine ophiolites (Italy): insights into the late-magmatic evolution of a MOR-type intrusive sequence. *Earth Planet. Sci. Lett.,* 176:281–293.

Vanko, D.A., and Stakes, D.S., 1991. Fluids in oceanic layer 3: evidence from veined rocks, Hole 735B, Southwest Indian Ridge. *In* Von Herzen, R.P., Robinson, P.T., et al., *Proc. ODP, Sci. Results,* 118: College Station, TX (Ocean Drilling Program), 181–215.

APPENDIX

Calculation Procedures of Amphibole Formula

It is impossible to determine the amount of Fe^{3+} and H_2O in amphiboles by microprobe analysis. Therefore, for calculation of amphibole formula, it is assumed, in general, that amphibole contains $O_{22}(OH,F,Cl)_2$ instead of 24 (O, OH, F, Cl) or 23 oxygen (Robinson et al., 1982).

The amount of Fe^{3+} can be arbitrarily calculated with several different assumptions, which include the assumption of all Fe as Fe^{2+} (all-Fe^{2+} method), adjustments of cations to 13 except Ca + Na + K (13eCNK method) and to 15 except Na + K (15eNK method), or the method proposed by Holland and Blundy (1994) (H&B method). Thus, we cannot uniquely calculate such important parameters for the terminology of amphibole (e.g., Leake et al., 1997) as Fe^{3+}, Al^{IV}, Al^{VI}, and A-site occupancy. This indicates the difficulty in comparing data from different literature in which the formula of amphiboles was calculated with different methods.

For the discussion of amphibole chemistry in this paper, we first calculated the cation numbers on a 23-oxygen basis. Then, we recalculated Fe^{3+} with the 13eCNK, 15eNK, and H&B methods. We discarded the results (two of 187 analyses) if either Fe^{2+} or Fe^{3+} were calculated to be negative or if Ca was allocated to either the M3 site or A-site. After these treatments, we compared the results by the different methods to choose appropriate formula by the following procedures.

Figure AF1 is $(Na + K)_{A\text{-site}}$ vs. Al^{IV} plots calculated by 13eCNK, 15eNK, and H&B methods. Also plotted are $(Na + K)_{A\text{-site}}$ calculated with the all-Fe^{2+} method. The plot of $(Na + K)_{A\text{-site}}$ with the all-Fe^{2+} method is the narrowest and falls very close to the pargasite–tremolite join. On the other hand, the results of 13eCNK are strongly scattered and show a shift toward lower Na + K and/or higher Al^{IV} directions. The results of 15eNK are plotted in a rather close position to the $(Na + K)_{A\text{-site}}$ calculated with the all-Fe^{2+} method, and those of the H&B method are plotted in the middle between the all-Fe^{2+}/15eNK results and 13eCNK results.

Cosca et al. (1991) compared the results provided by the several methods with amphiboles from amphibolites and granulites of the Grenville Orogen of Ontario. Their examinations indicate that the 13eCNK method provided the best results. Following their results, we evaluated our data with the assumption that the 13eCNK method provides the best formula. If so, the wide scatter of the 13eCNK results should not be accidental but meaningful. If this is true, the apparent tight distribution of $(Na + K)_{A\text{-site}}$ calculated with the all-Fe^{2+} method to the pargasite–tremolite join would have to be accidentally given by incomplete microprobe analyses or inappropriate corrections. We do not think this is the case. The tight distribution of the $(Na + K)_{A\text{-site}}$ data to the pargasite–tremolite tie line is more likely to be true than the wide and nonsystematically scattered results of the 13eCNK method. Figure AF2 shows $Fe^{3+}/(Fe^{2+}+Fe^{3+})$ vs. Mg# (100 × Mg/[Mg+Fe^{2+}+Fe^{3+}]) and $Fe^{3+}/(Fe^{2+}+Fe^{3+})$ vs. Si. At a given Mg# and/or Si values, plots of $Fe^{3+}/(Fe^{2+}+Fe^{3+})$ ratios calculated with the 13eCNK method are strongly scattered. It is not easy to explain these large dispersions. It is possible that there was pervasive but incomplete later-stage oxidation or an analyti-

AF1. $(Na + K)_{A\text{-site}}$ vs. Al^{IV} of amphiboles, p. 41.

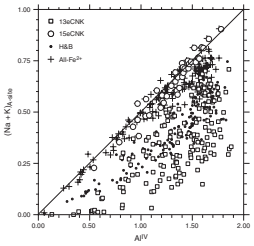

AF2. $Fe^{3+}/(Fe^{2+}+Fe^{3+})$ vs. Mg# (100 × Mg/[Mg+Fe]) and $Fe^{3+}/(Fe^{2+}+Fe^{3+})$ vs. Si, p. 42.

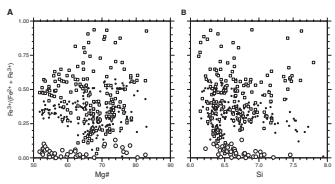

cal problem, but it is most likely that the dispersion is an artifact of the correction scheme.

Based on these examinations, we have concluded that the 13eCNK method does not yield good results for our purposes in this research. The order of priority we took is 15eNK, all-Fe^{2+}, H&B, and then 13eCNK methods. All the data accepted here are those calculated with the 15eNK (39 analyses) or all-Fe^{2+} methods (146 analyses). These procedures resulted in rather low $Fe^{3+}/(Fe^{2+}+Fe^{3+})$ ratios. Average, standard deviation, maximum, and minimum values of the $Fe^{3+}/(Fe^{2+}+Fe^{3+})$ ratio of 39 analyses calculated using the 15eNK method were 0.0439, 0.0326, 0.1315, and 0.0001, respectively.

Figure F1. Downhole distributions of the high-temperature microscopic veins and interfingering textures of clinopyroxene. We have no data on the veins and interfingering texture for the upper 500 m interval of Hole 735B cored during Leg 118. **A.** Occurrence of the high-temperature microscopic veins shown in horizontal lines. Solid circles = Mg# (mol) of normative mafic silicate calculated for the cored samples of Hole 735B. **B.** Occurrence of the interfingering texture of clinopyroxene is shown by horizontal lines. Solid circles = An% (mol) of normative plagioclase of the cored samples. Whole-rock data for normative calculation are from Robinson, Von Herzen, et al. (1989) and Dick, Natland, Miller, et al. (1999). In the calculation, Fe^{3+} was assumed as 0.1 total Fe. Basaltic and diabasic rocks, felsic veins, and strongly altered rocks are not included in the normative calculations.

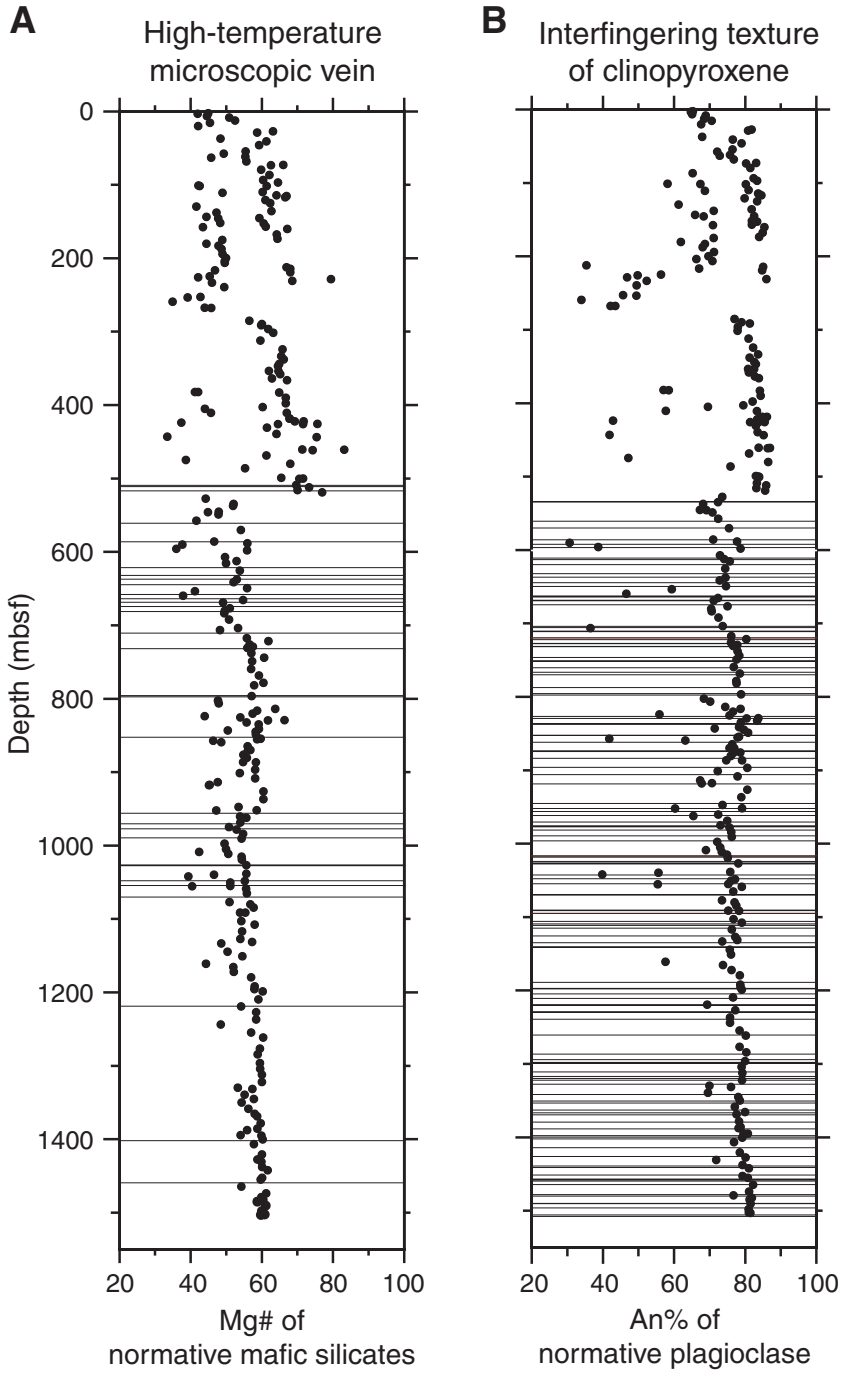

Figure F2. Photomicrographs of the examined olivine gabbros. **A, B.** Olivine gabbro (Sample 176-735B-101R-1 [Piece 7, 106–108 cm]; (A) cross-polarized and (B) plane-polarized light; field of view = 1.4 cm). (Continued on next page.)

A

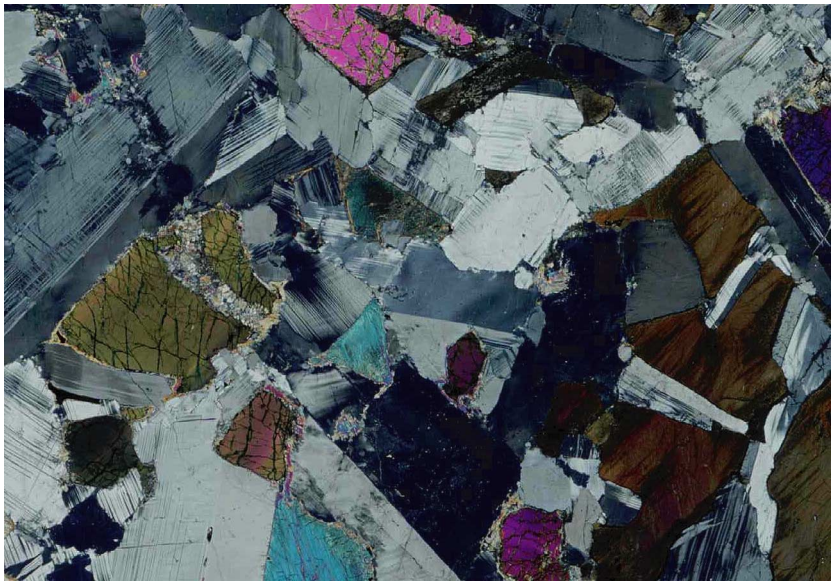

B

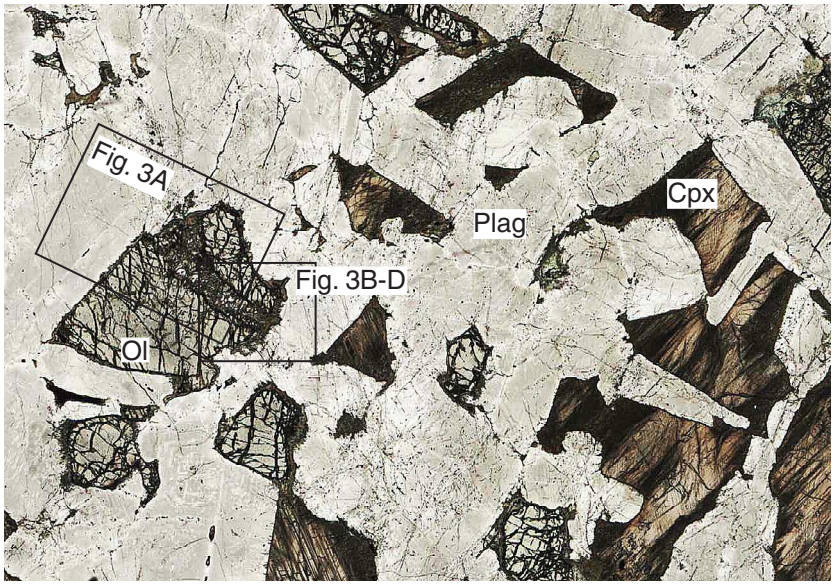

Figure F2 (continued). C, D. Olivine gabbro (Sample 176-735B-156R-3 [Piece 5, 51–54 cm]; (C) cross-polarized and (D) plane-polarized light; field of view = 1.4 cm). Ol = olivine, Plag = plagioclase, Cpx = Ca-rich clinopyroxene.

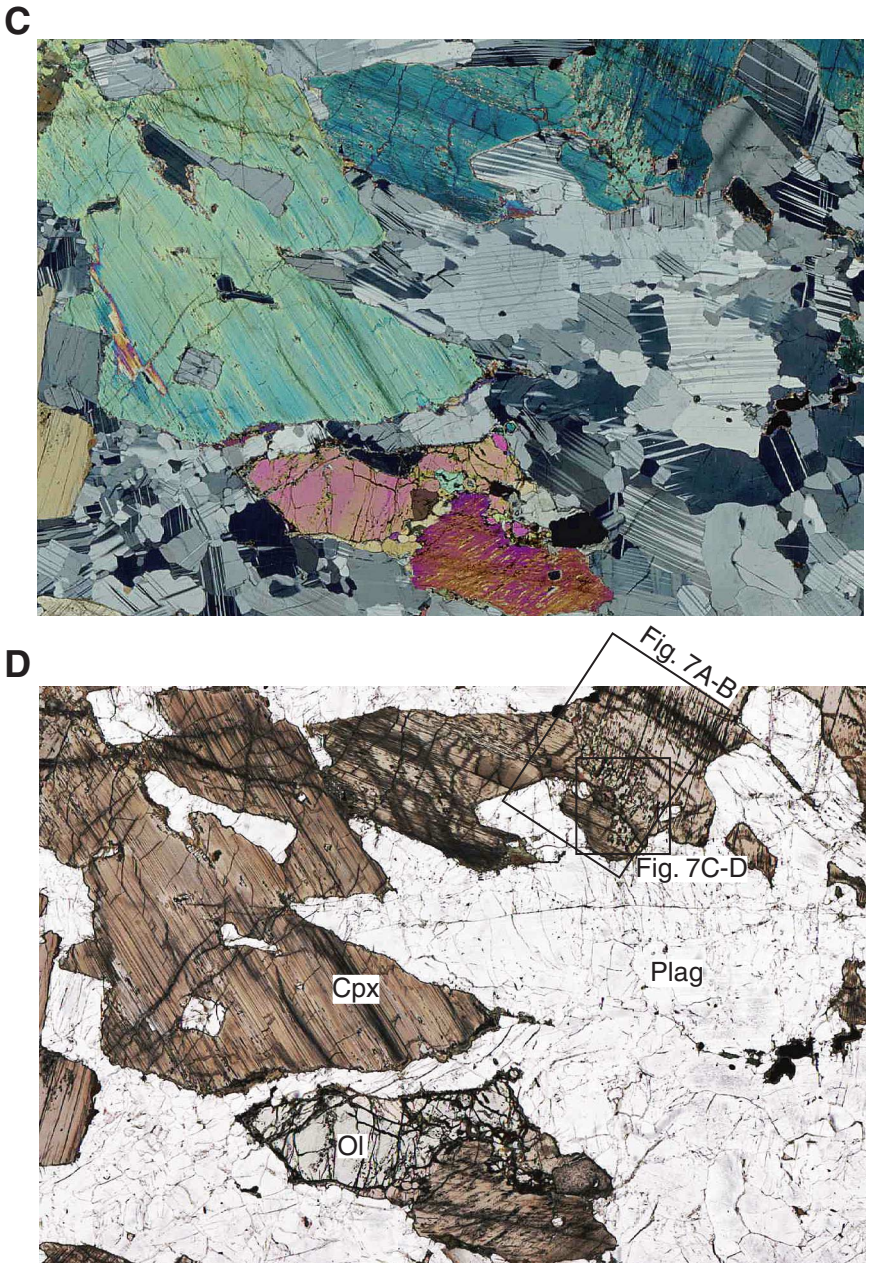

Figure F3. Occurrence of the high-temperature microscopic veins (HTMV). **A.** Photomicrograph of a high-temperature microscopic vein penetrating magmatic grains of olivine (Ol) and plagioclase (Plag) in olivine gabbro (Sample 176-735B-101R-1 [Piece 7, 106–108 cm]; cross-polarized light; field of view = 3.2 mm). See also Figure F2B, p. 23, for location of the vein. **B.** Mg compositional map. (Continued on next page.)

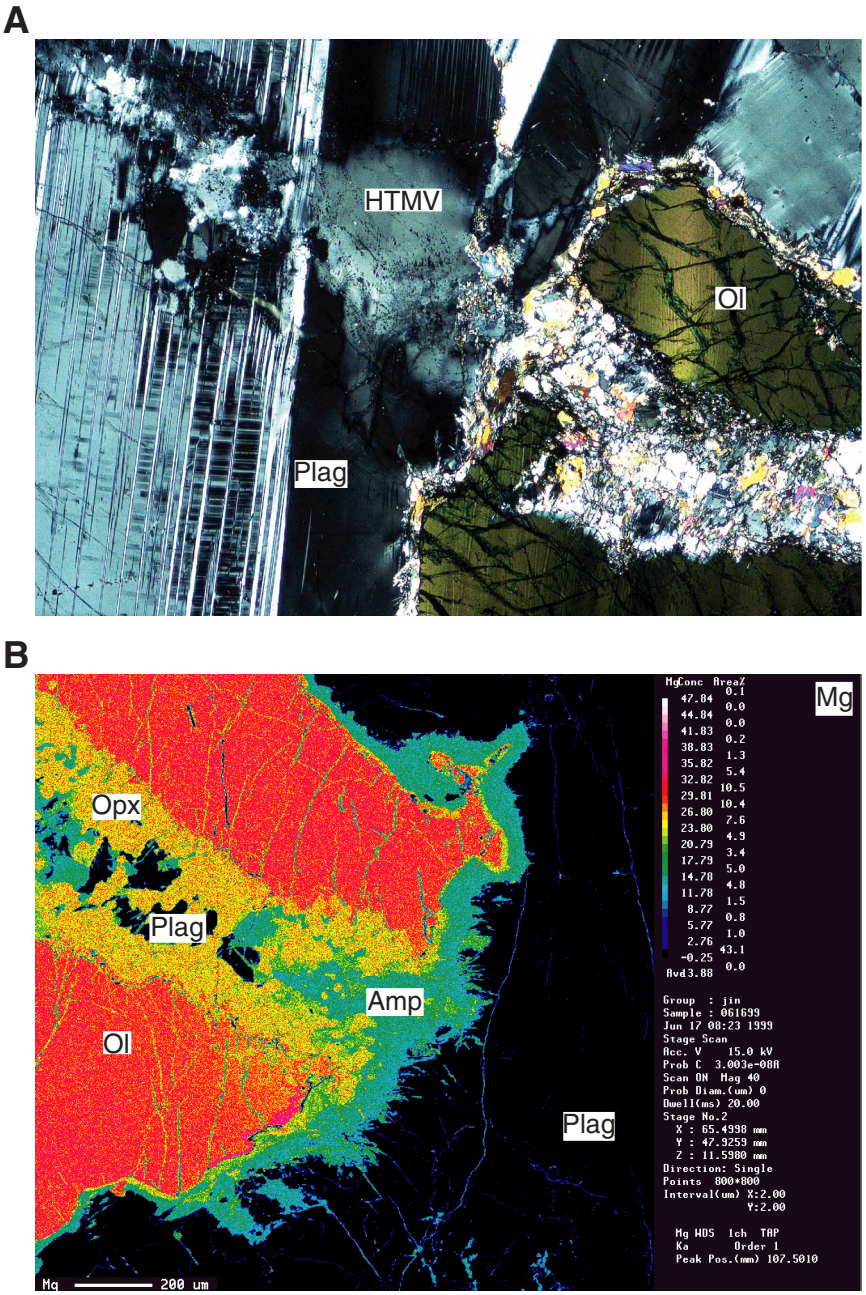

Figure F3 (continued). C, D. Compositional map: (**C**) Ca, and (**D**) Al. Ol = olivine, Plag = plagioclase, CPlag = calcic plagioclase, LCPlag = less calcic plagioclase, Opx = orthopyroxene, Amp = amphibole. Scale bars = 200 µm. Calcic plagioclase and amphibole are not distinguished in (C) due to their similar Ca contents. Note the calcic and less-calcic plagioclase grains within the vein and their irregular-shaped boundary (C) and (D).

C

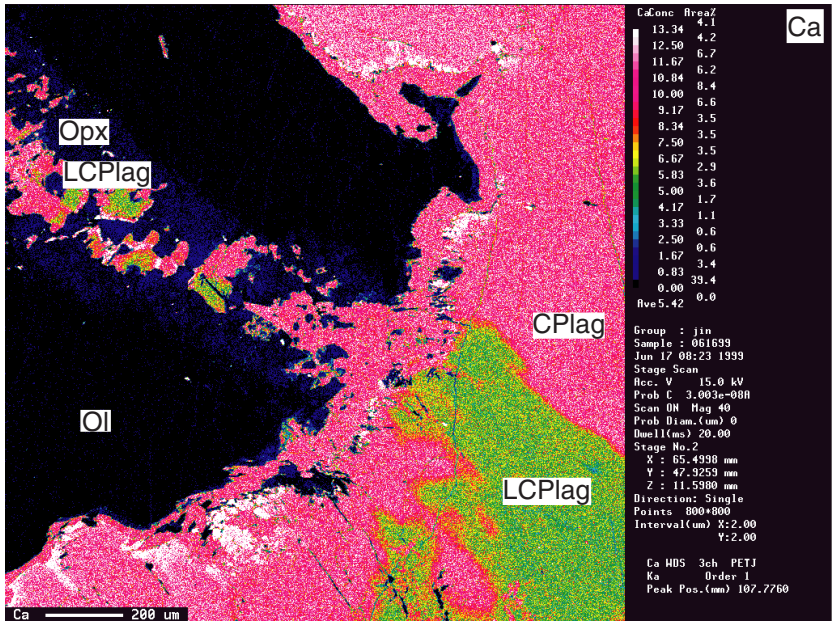

D

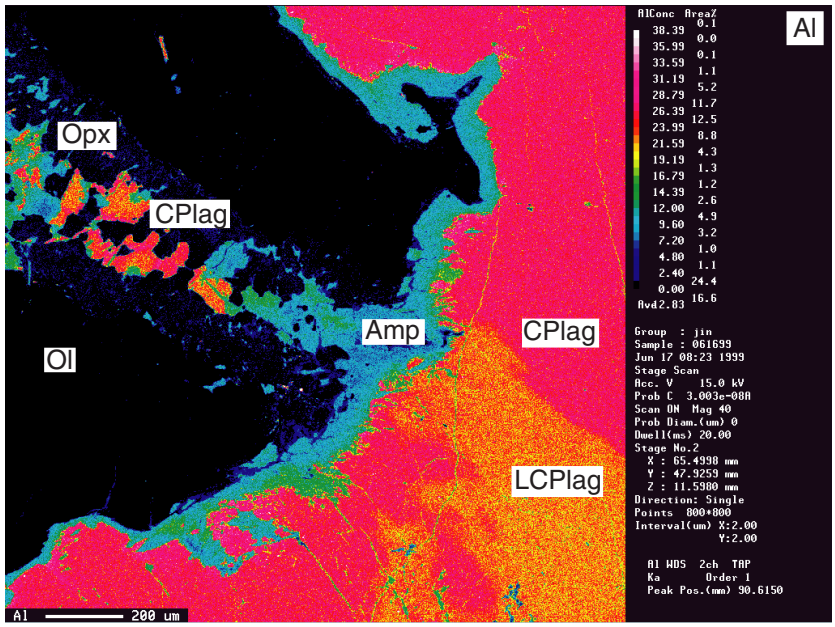

Figure F4. Histogram showing An% of plagioclase of magmatic origin and within the veins (Sample 176-735B-101R-1 [Piece 7, 106–108 cm]). Although a bimodal distribution is clearly shown, calcic plagioclase is also observed in the veins. Data (n = 114) are from the area around the olivine grain shown in Figure F3, p. 25.

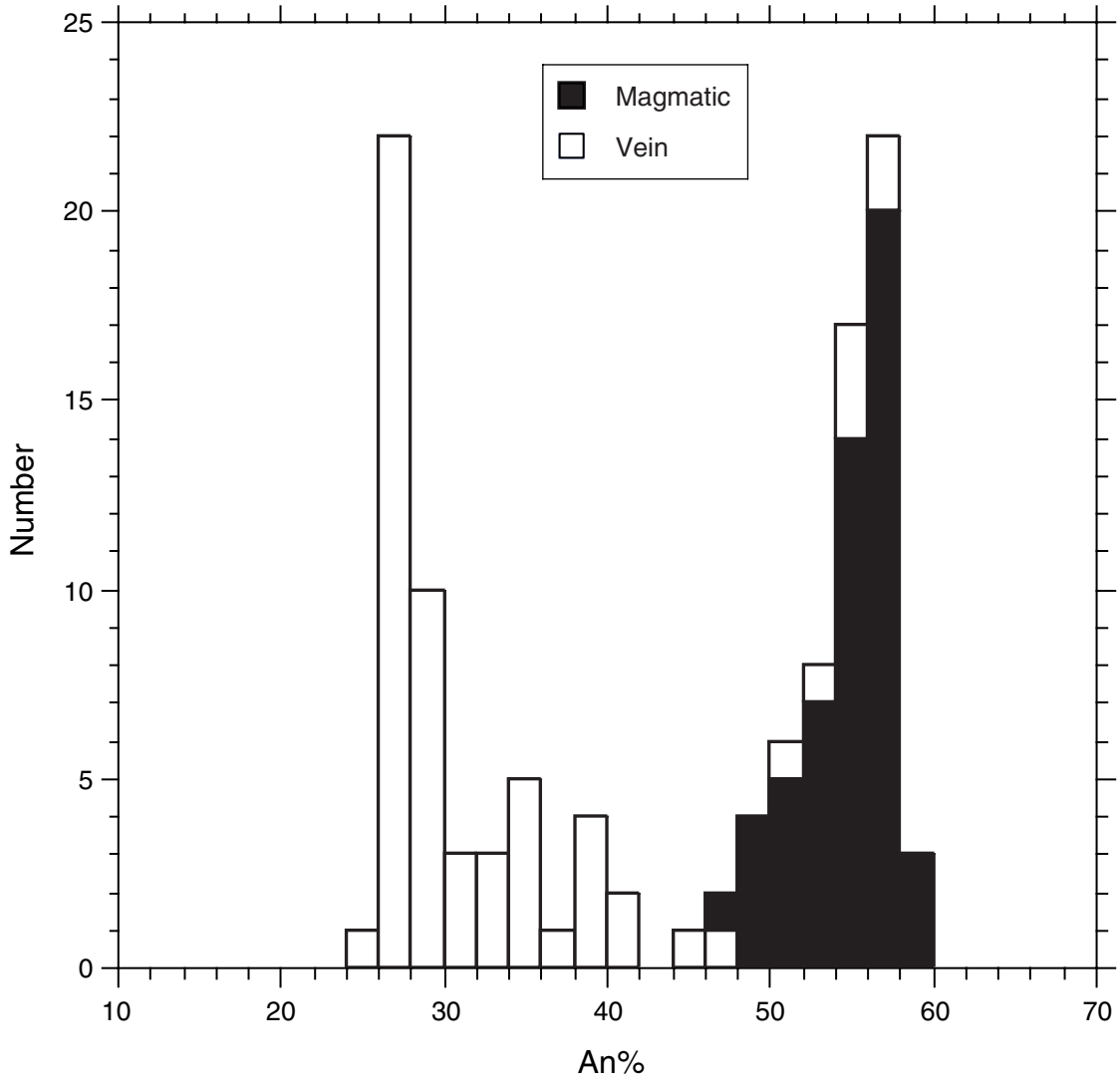

Figure F5. Occurrence of the high-temperature microscopic veins (HTMV). **A, B.** Photomicrograph of a high-temperature microscopic vein cutting olivine, clinopyroxene, and plagioclase in olivine gabbro (Sample 176-735B-130R-3 [Piece 11, 93–95 cm]; (A) cross-polarized and (B) plane-polarized light; field of view = 6.4 mm). In these figures, two high-temperature microscopic veins are shown from upper left to lower right. In the grain of clinopyroxene (Cpx), these high-temperature microscopic veins are marked by the discontinuous alignment of brown amphiboles. The lower vein penetrates an olivine grain (Ol). The upper vein is filled by amphibole within the grains of plagioclase, which is cut by the "later amphibole" vein (LAV), which runs vertically with amphibole (RepAmp) replacing magmatic clinopyroxene. Note the "later amphibole vein" is accompanied by a small offset shown by twinning of magmatic plagioclase (Plag).

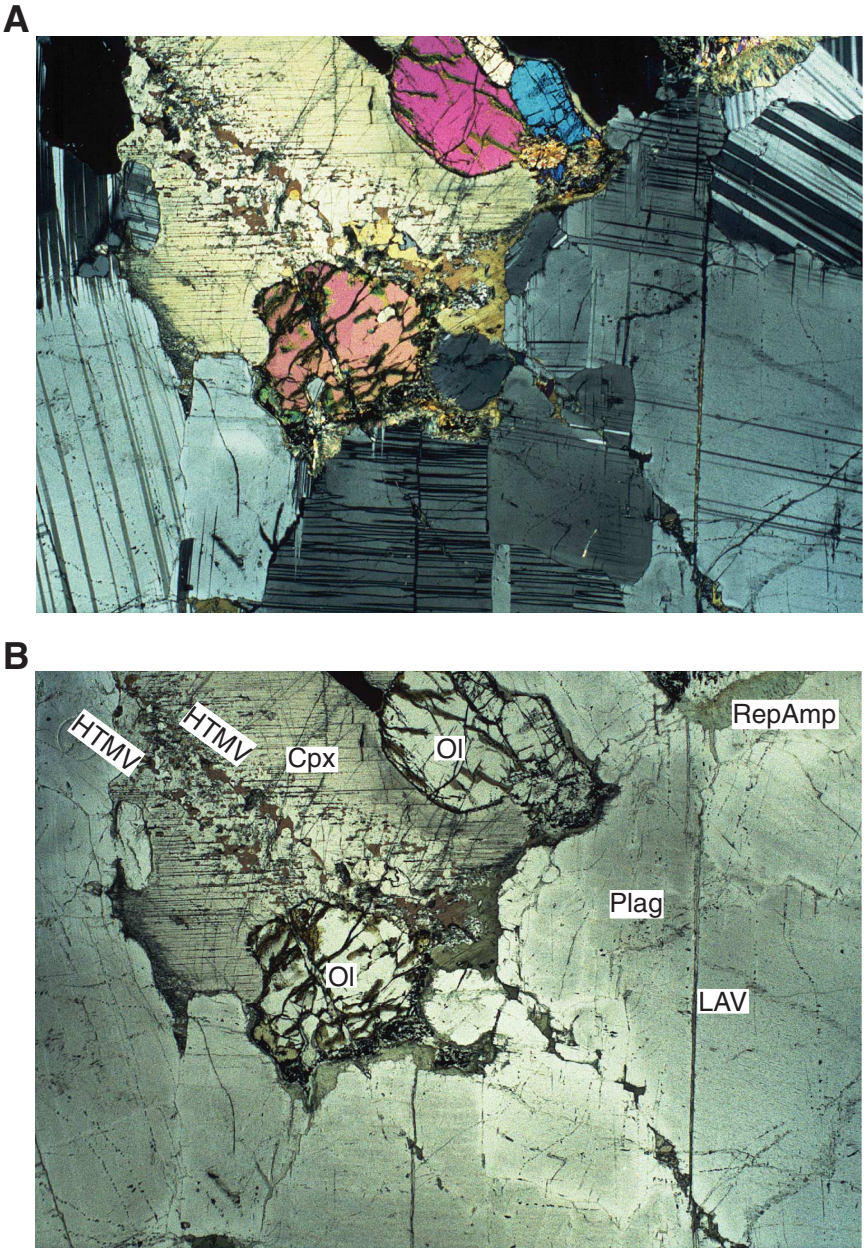

Figure F6. Occurrence of the high-temperature microscopic vein (HTMV) with intergrowths. Photomicrograph of a high-temperature microscopic vein cutting a clinopyroxene (Cpx) oikocryst and plagioclase (Plag) chadacryst in olivine gabbro (Sample 176-735B-156R-3 [Piece 5, 51–54 cm]). **A.** Cross-polarized light; field of view = 3.2 mm. **B.** Plane-polarized light; field of view = 1.3 mm. The rectangle shown in (A) shows the location of (B). The high-temperature microscopic vein is running from upper left to lower right in these figures. Note the symmetrical occurrence of intergrowths (Ig) of brown amphibole (Amp) + orthopyroxene (Opx) on both sides of the high-temperature microscopic vein (B). This clinopyroxene oikocryst includes three irregular-shaped grains of clinopyroxene (IfIg) which show vermicular or symplectitic intergrowth of brown amphibole + orthopyroxene. These are interfingering textures cut in different directions from those shown in Figure F7C and F7D, p. 32. (Continued on next page.)

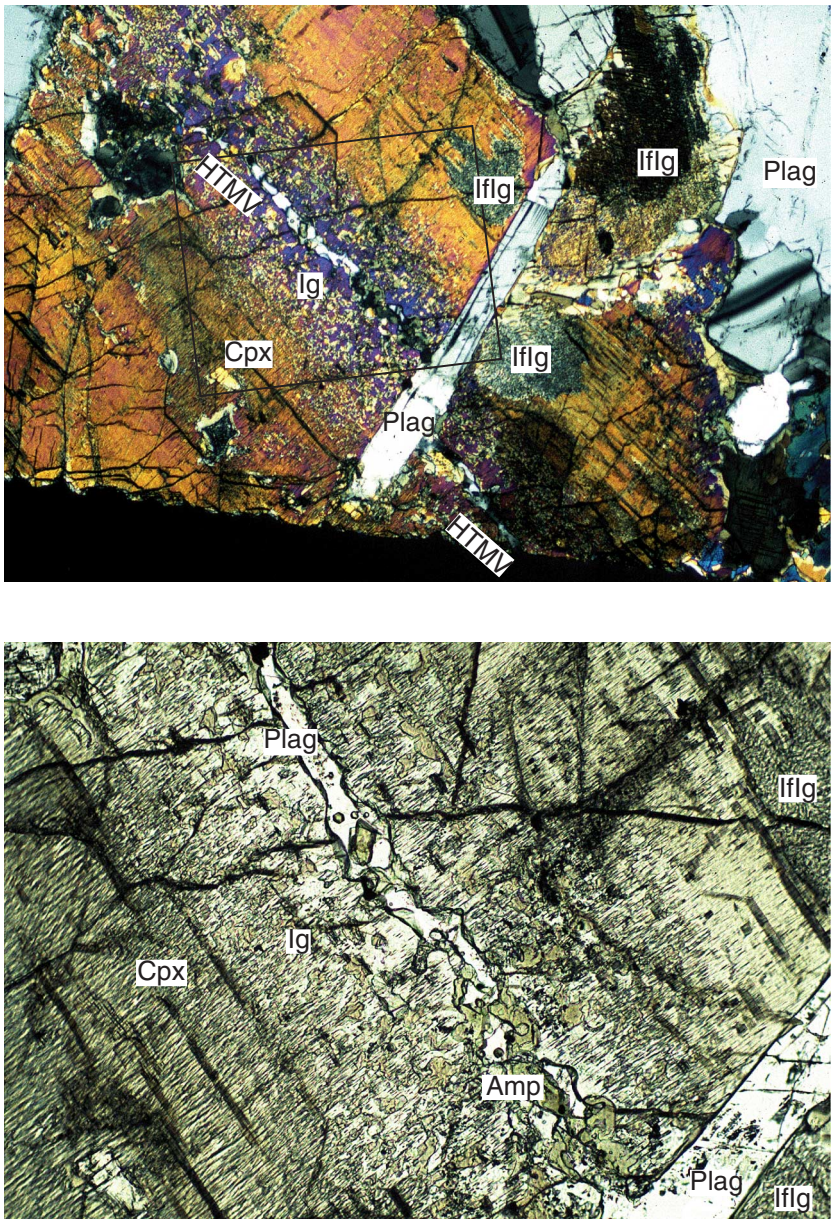

Figure F6 (continued). C, D. Compositional map of this area: (C) Ca and (D) Al; scale bars = 200 µm. Note the compositional difference between calcic chadacrystic plagioclase and less calcic plagioclase of the vein (C) and compositional differences in Ca and Mg within the grain of clinopyroxene (C and D). Calcic plagioclase and amphibole are not distinguished in (C) due to their similar Ca contents. LCPlag = less calcic plagioclase, IfIg = interfingering intergrowth.

C

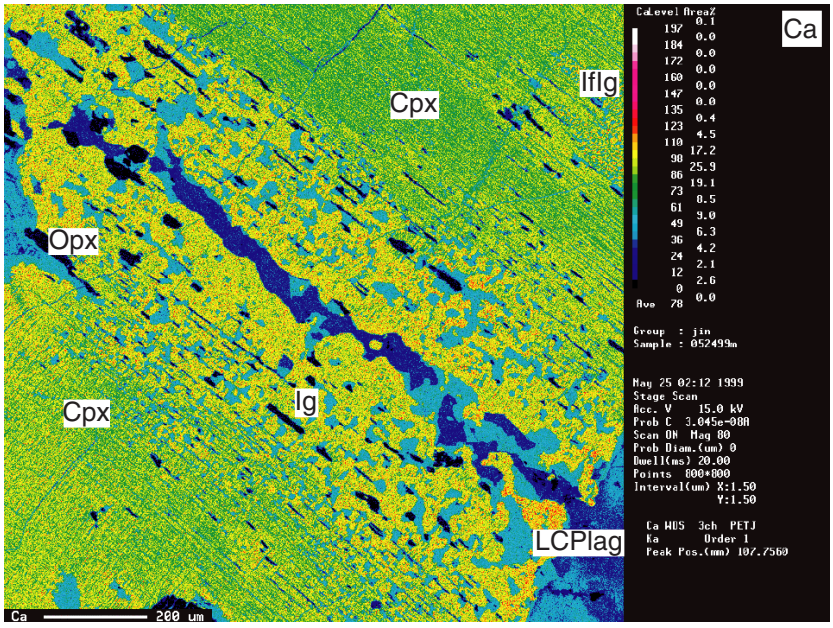

D

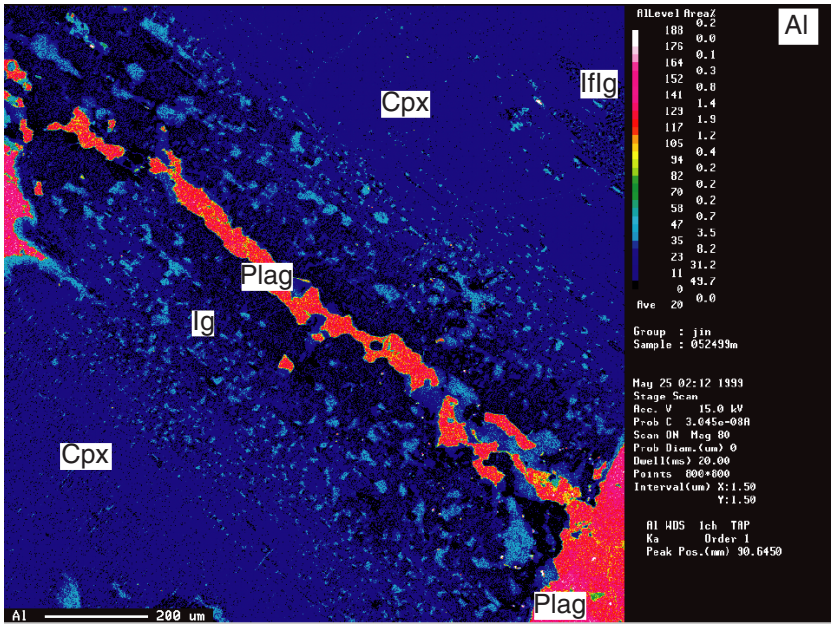

Figure F7. Occurrence of the interfingering texture of clinopyroxene in olivine gabbro. See Figure F2D, p. 23, for the location of this area. **A, B.** Photomicrograph of the interfingering texture of clinopyroxene in olivine gabbro (Sample 176-735B-156R-3 [Piece 5, 51–54 cm]; (A) cross-polarized and (B) plane-polarized light; field of view = 3.2 mm). The interfingering part of the grains of clinopyroxene (Cpx) contains an intergrowth of brown amphibole (Amp) + orthopyroxene (Opx). The interfingering clinopyroxene hosting the intergrowth looks clear under the microscope. (Continued on next page).

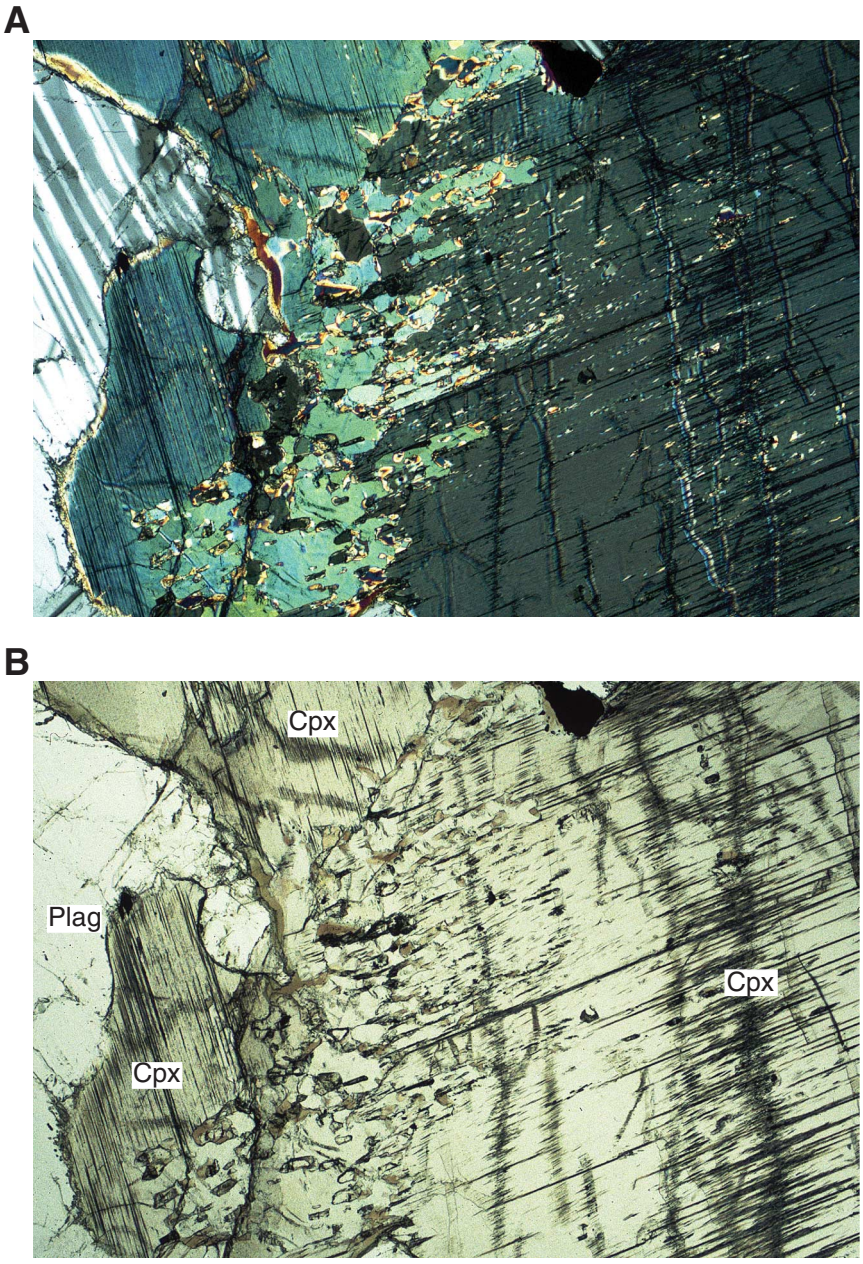

Figure F7 (continued). C, D. Compositional map of this area: (C) Ca and (D) Al; scale bars = 200 µm. Note the compositional difference between two areas within clinopyroxene grain (i.e., with and without the intergrowth). Calcic plagioclase and amphibole are not distinguished in (C) because of their similar Ca contents.

C

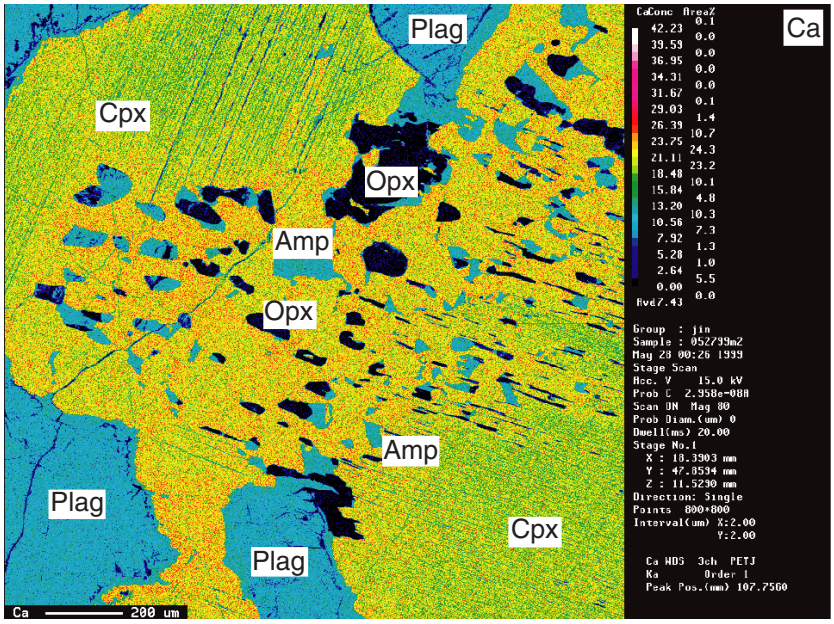

D

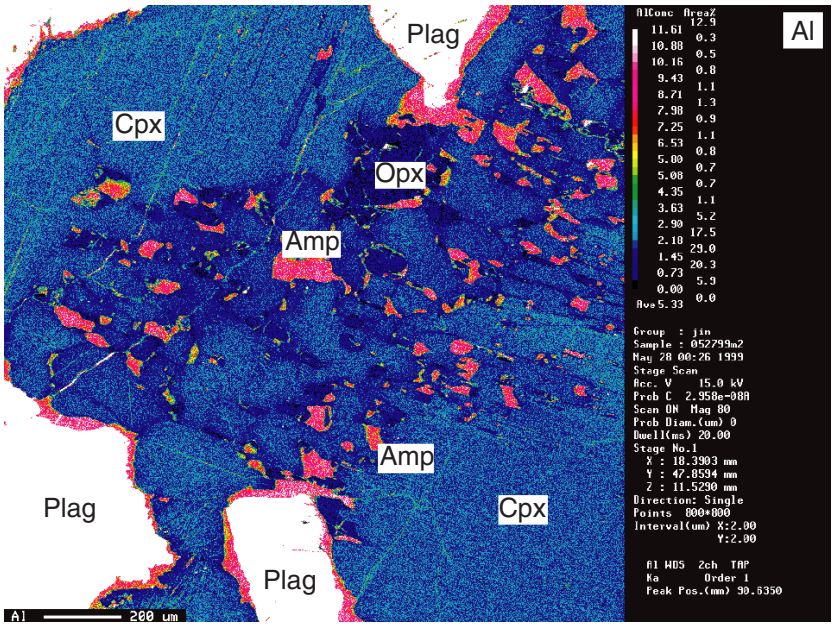

Figure F8. Pyroxene quadrilateral. Clinopyroxenes are classified into magmatic, interfingering, and near the veins. Orthopyroxenes are classified into magmatic rims, blebs in the interfingering clinopyroxene, blebs near the veins, and veins within olivine grains.

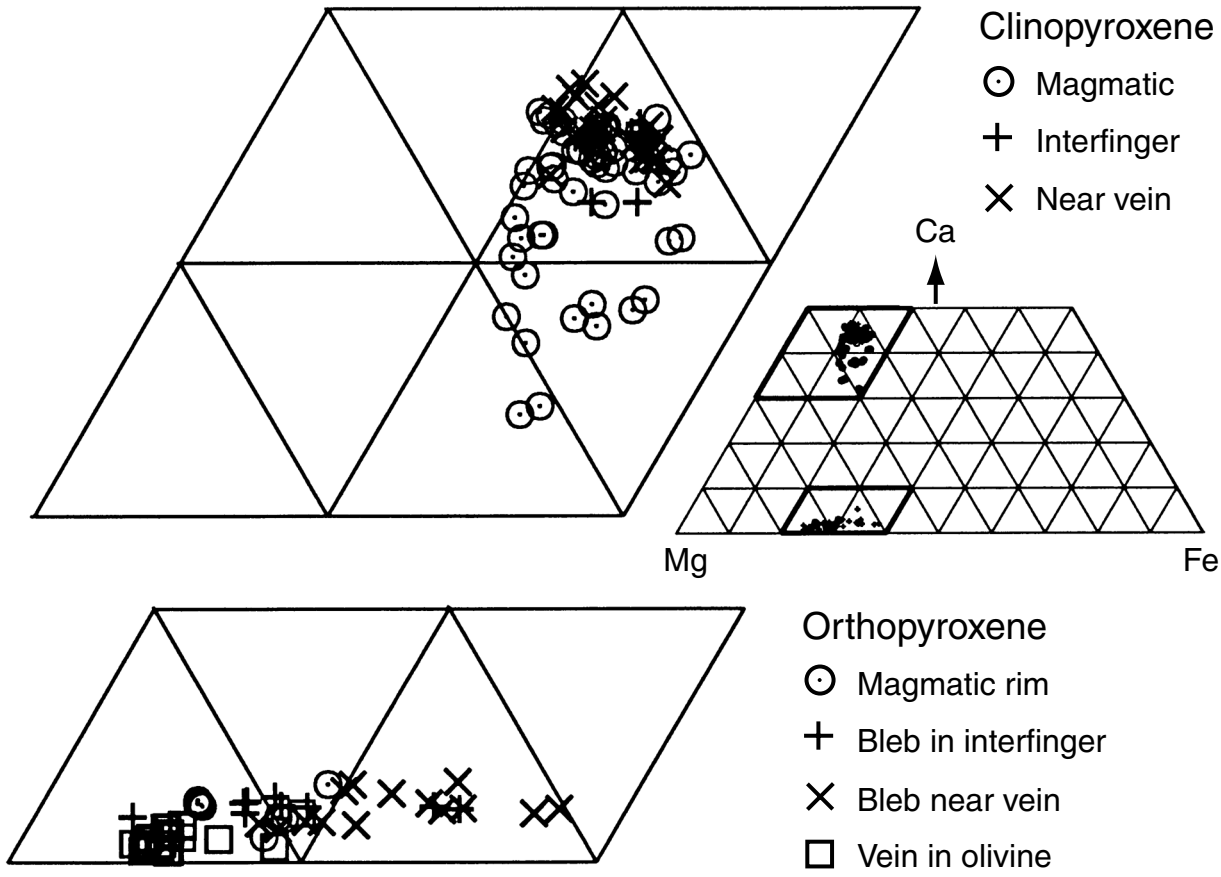

Figure F9. Composition of clinopyroxene. **A.** Al_2O_3 vs. Mg#. **B.** TiO_2 vs. Mg#. **C.** TiO_2 vs. Al_2O_3. Clinopyroxenes hosting the intergrowth of brown amphibole + orthopyroxene near the high-temperature microscopic veins are clearly lower in Al_2O_3 and TiO_2 than those of the magmatic clinopyroxenes. The interfingering clinopyroxenes hosting the intergrowth of brown amphibole + orthopyroxene are plotted between those of magmatic clinopyroxenes and clinopyroxenes near the high-temperature microscopic veins.

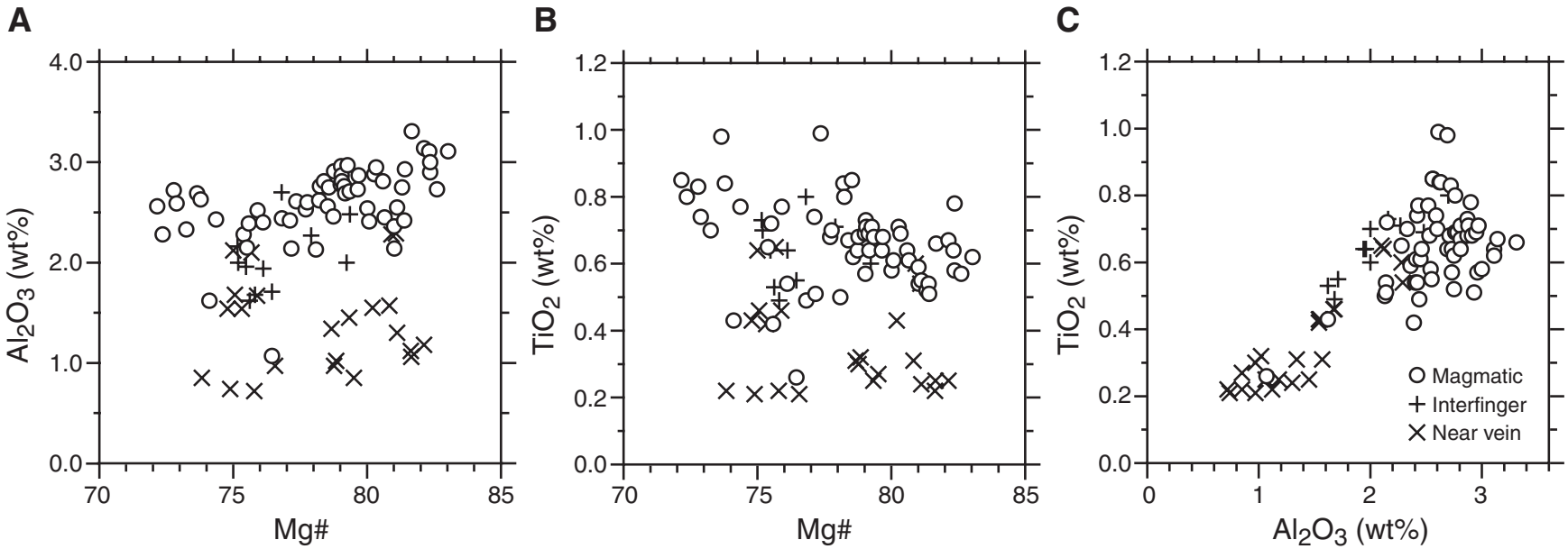

Figure F10. Composition of orthopyroxene. **A.** TiO_2 vs. Al_2O_3. **B.** TiO_2 vs. CaO. For orthopyroxenes, there is no essential compositional difference among the magmatic orthopyroxenes and those of blebs in the intergrowths (near the high-temperature microscopic veins and in the interfingering clinopyroxene), except for grains within the high-temperature microscopic veins in olivine. The latter are characterized by lower contents of CaO, TiO_2, and Al_2O_3 than other orthopyroxenes. These compositional features are attributed to the Ca-, Ti-, and Al-poor nature of olivine, which is a precursor of the orthopyroxene.

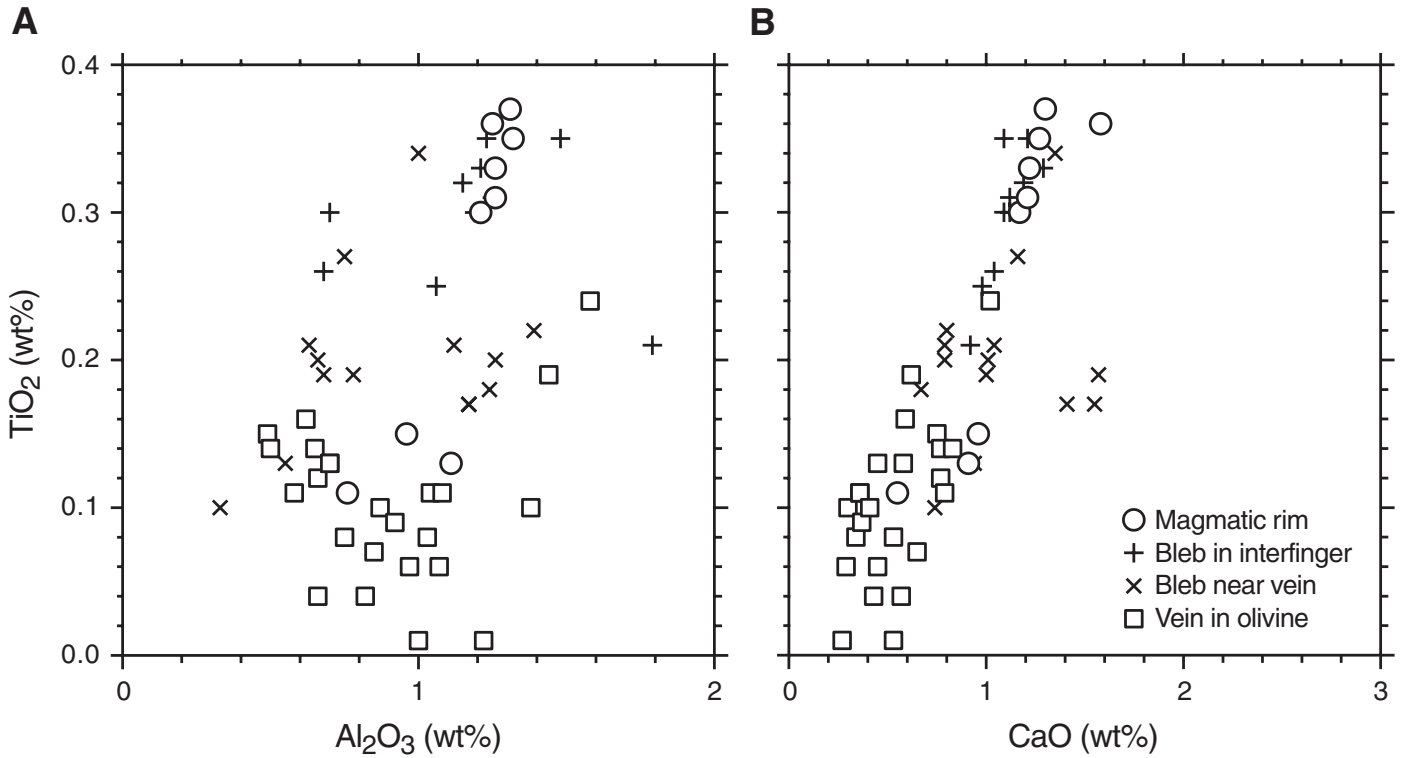

Figure F11. Composition of amphiboles. **A.** $(Na + K)_{A\text{-site}}$ vs. Al^{IV} (per formula unit). **B.** Mg# vs. Al^{IV}. **C.** Ti vs. Al^{IV}. The calculation procedures of the amphibole formula are given in the **"Appendix,"** p. 20. The terminology of amphiboles is after Leake et al. (1997). Most of the analyses are plotted on the join between pargasite and tremolite. Note that the amphiboles from the high-temperature microscopic veins penetrating olivine grains are characteristically low in Ti content compared to those within clinopyroxene grains (C). (**Figure shown on next page.**)

Figure F11 (continued). (Caption shown on previous page.)

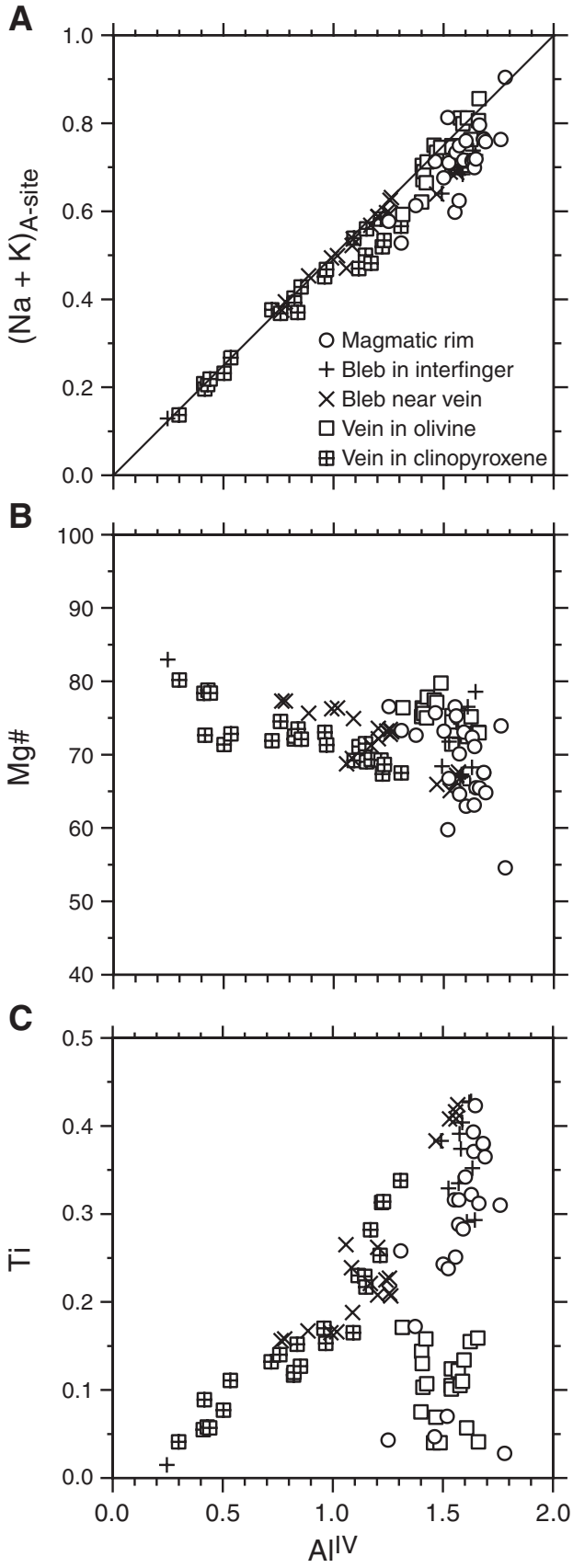

Figure F12. Temperatures calculated for clinopyroxene, orthopyroxene, and amphibole-plagioclase. Pyroxene temperatures are calculated with the thermometer proposed by Lindsley and Anderson (1983), and amphibole-plagioclase temperatures calculated with the thermometer proposed by Holland and Blundy (1994). **1.** Sample 176-735B-101R-1 (Piece 7, 106–108 cm), **2.** Sample 176-735B-112R-2 (Piece 1, 64–66 cm), **3.** Sample 176-735B-130R-3 (Piece 11, 93–95 cm), **4.** Sample 176-735B-156R-3 (Piece 5, 51–54 cm).

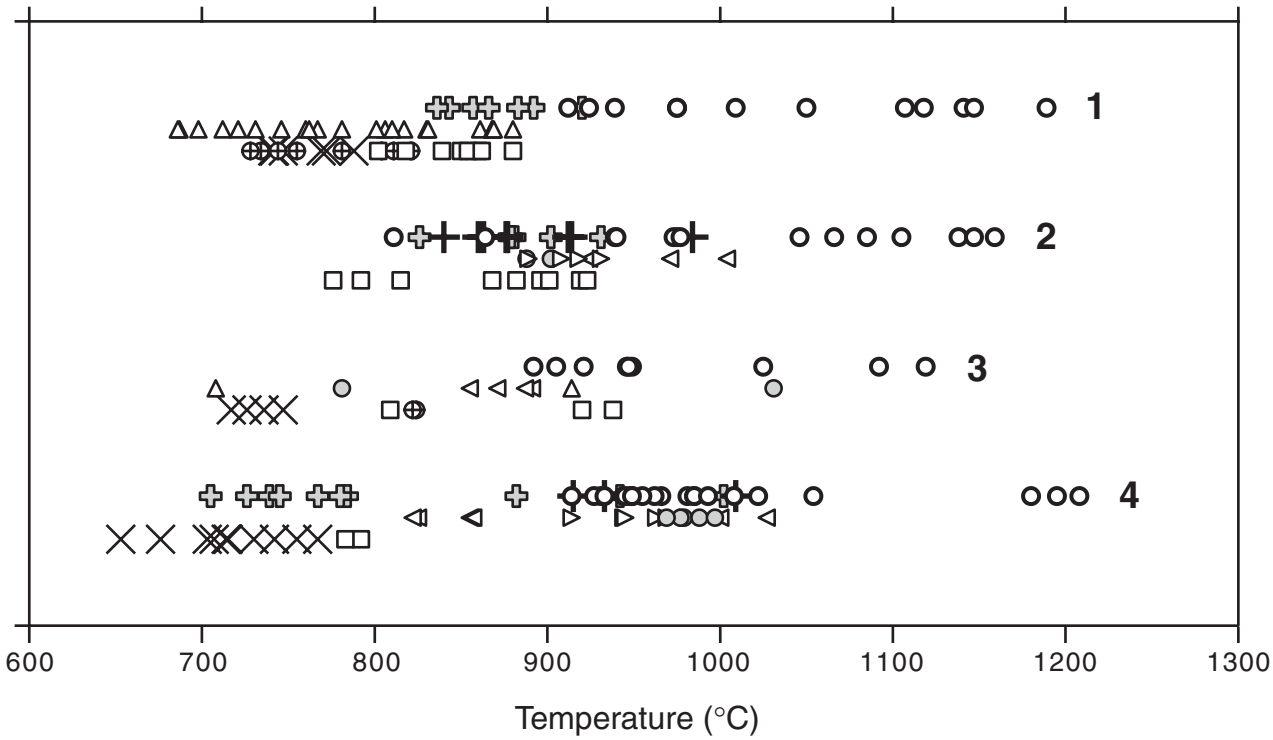

Figure F13. Photomicrographs of olivine gabbros. **A.** Intimate association of the high-temperature microscopic veins (HTMV) and the interfingering texture of clinopyroxene (Sample 176-735B-112R-2 [Piece 1, 64–66 cm]; cross-polarized light; field of view = 3.2 mm). The high-temperature microscopic vein is marked by discontinuous alignment of brown amphibole (Amp) in clinopyroxene (Cpx) in the lower left. The interfingering clinopyroxene (center) hosts the intergrowth (IfIg) and looks clear under the microscope. **B.** Clinopyroxene porphyroclast showing the interfingering texture in deformed olivine gabbro (Sample 176-735B-148R-1 [Piece 2, 104–112 cm]; cross-polarized light; field of view = 6.4 mm). Note the intergrowth (IfIg) of brown amphibole + orthopyroxene in clinopyroxene porphyroclast. (Continued on next page.)

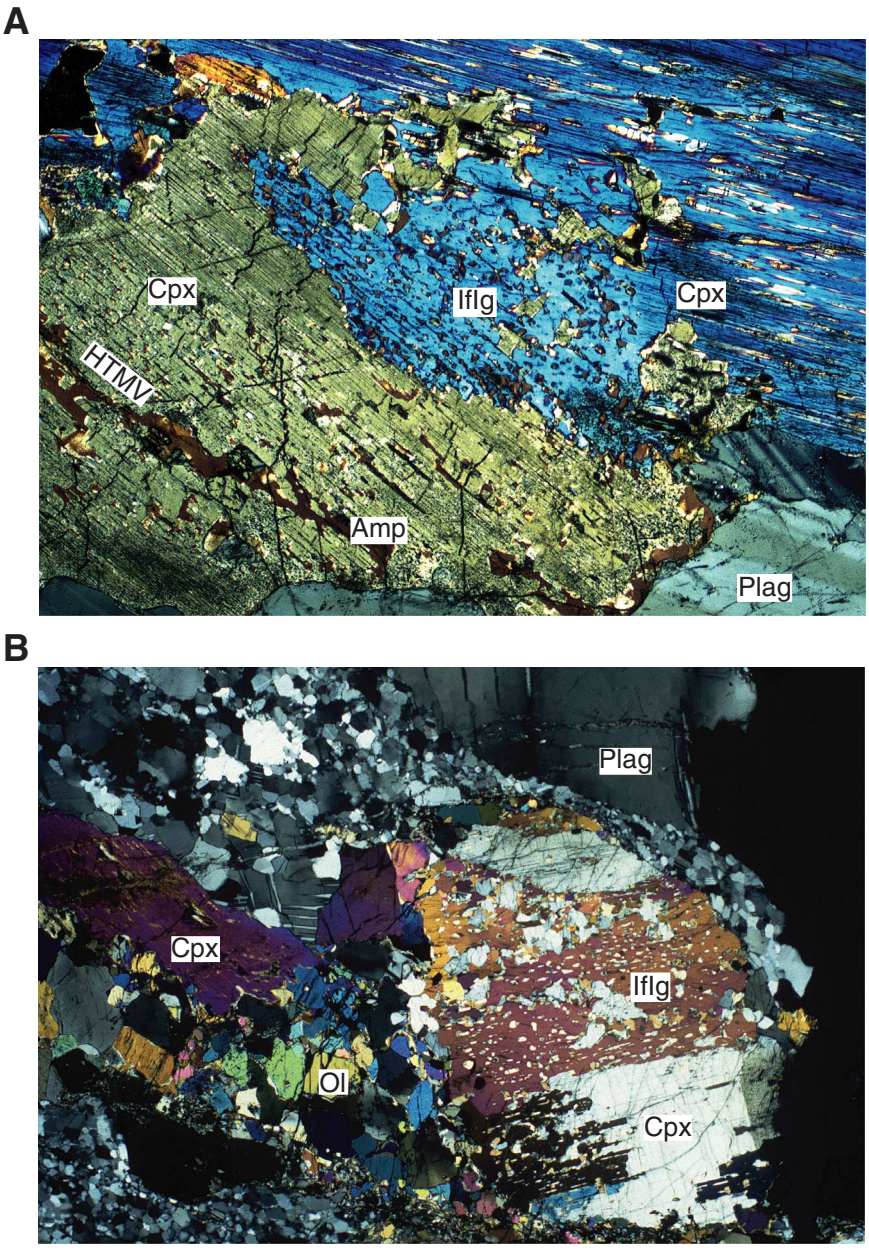

Figure F13 (continued) C. High-temperature microscopic vein (HTMV) along the grain boundary between plagioclase and clinopyroxene in olivine gabbro (Sample 176-735B-101R-1 [Piece 7, 106–108 cm]; cross-polarized light; field of view = 3.2 mm). The vein is running on the outer edge of the magmatic plagioclase grain. A very fine grained intergrowth of brown amphibole + orthopyroxene (Ig) was formed on the edge of the clinopyroxene contacted by the vein. In this figure, also shown is the intimate association of high-temperature microscopic veins and the interfingering clinopyroxene (IfIg). Ol = olivine, Cpx = Ca-rich clinopyroxene, Plag = plagioclase.

C

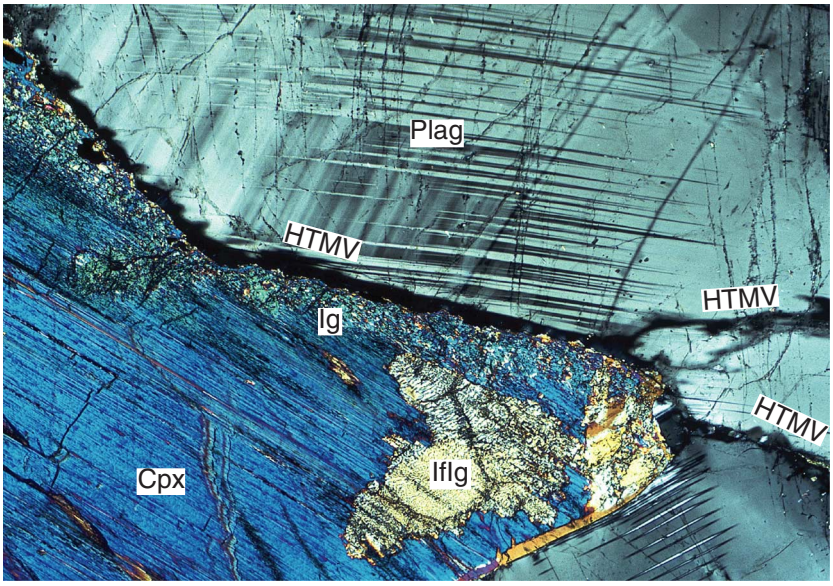

Figure AF1. $(Na + K)_{A\text{-site}}$ vs. Al^{IV} (per formula unit) of amphiboles analyzed in this study. Squares = 13eCNK, open circles = 15eCNK, solid circles = H&B, crosses = all-Fe^{2+} methods.

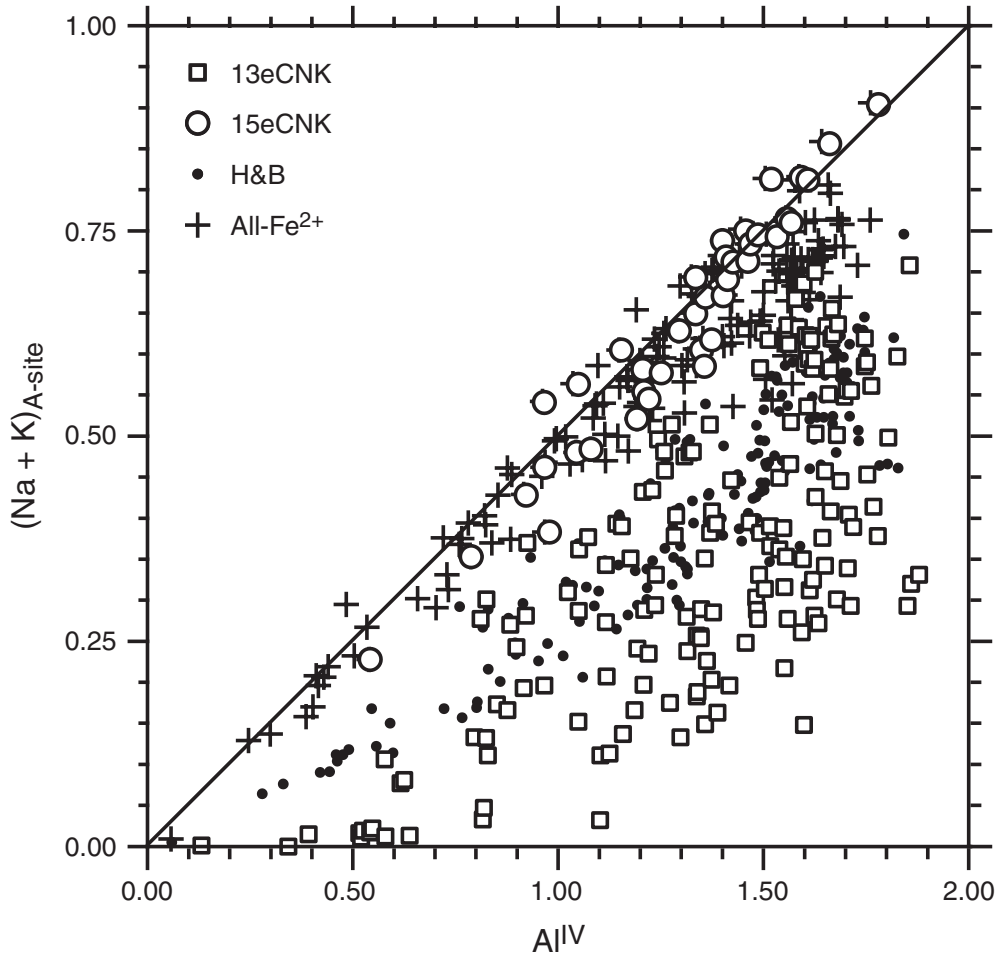

Figure AF2. $Fe^{3+}/(Fe^{2+}+Fe^{3+})$ vs. Mg# (100 × Mg/[Mg+Fe]) and $Fe^{3+}/(Fe^{2+}+Fe^{3+})$ vs. Si (per formula unit) of amphiboles analyzed in this study. Squares = 13eCNK, open circles = 15eCNK, solid circles = H&B, crosses = all-Fe^{2+} methods.

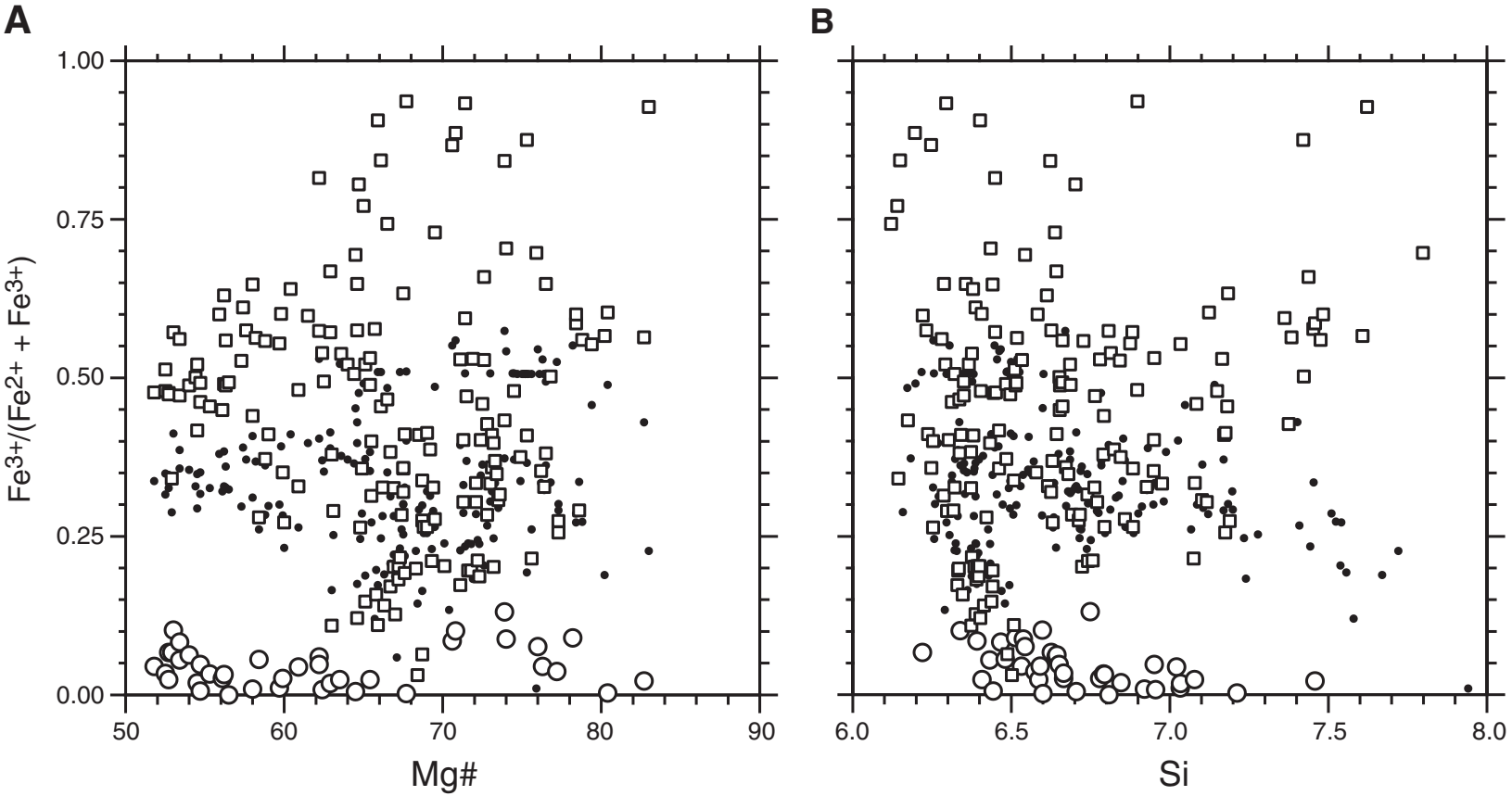

Table T1. Occurrence of high-temperature microscopic veins.

	Troctolite	Olivine gabbro and gabbro	Oxide-rich gabbros	Microgabbros	Felsic veins	All samples
Presence	3 (27.3%)	26 (15.8%)	2 (12.5%)	0 (0.0%)	0 (0.0%)	31 (14.3%)
Absence	8 (72.7%)	139 (84.2%)	14 (87.5%)	24 (100.0%)	1 (100.0%)	186 (85.7%)
Total	11	165	16	24	1	217

Table T2. Samples containing high-temperature microscopic veins.

Core section, interval (cm)	Depth (mbsf)	Lithology
176-735B-		
90R-2 (Piece 1, 10–12)	509.40	TG
90R-3 (Piece 1, 22–24)	510.99	TG
90R-7 (Piece 1, 80–82)	516.73	TG
97R-4 (Piece 3, 65–67	560.81	OG
101R-1 (Piece 7, 106–108)	586.16	OG
107R-2 (Piece 1, 60–62)	621.52	OXG
109R-3 (Piece 3, 69–71)	632.17	OG
110R-3 (Piece 4, 107–109)	637.07	OG
112R-2 (Piece 1, 64–66)	644.62	OG
114R-4 (Piece 3, 113–115)	657.84	OXG
115R-2 (Piece 1, 44–47)	663.94	OG
115R-5 (Piece 2, 83–85)	668.51	OG
116R-3 (Piece 1, 22–24)	674.49	OG
117R-1 (Piece 2, 10–12)	681.30	OG
120R-1 (Piece 3, 47–51)	710.47	OG
122R-2 (Piece 4, 106–108)	731.76	OG
130R-2 (Piece 4, 47–51)	795.66	OG
130R-3 (Piece 11, 93–95)	797.57	OG
137R-1 (Piece 3, 72–74)	852.52	OG
148R-4 (Piece 5, 89–91)	956.16	OG
149R-8 (Piece 3, 116–120)	970.41	OG
150R-6 (Piece 1, 39–41)	977.17	OG
152R-2 (Piece 1, 52–54)	989.47	OG
156R-3 (Piece 5, 51–54)	1027.59	OG
156R-2 (Piece 2, 75–79)	1026.38	OG
158R-3 (Piece 5, 117–119)	1047.88	OG
159R-1 (Piece 8, 83–87)	1054.53	OG
160R-5 (Piece 3, 97–99)	1070.02	OG
178R-6 (Piece 4, 76–81)	1218.82	OG
200R-1 (Piece 1, 3–9)	1402.03	OG
205R-7 (Piece 4, 73–75)	1459.59	OG

Note: TG = troctolites, OG = olivine gabbros and gabbros, OXG = oxide-rich gabbros.

Table T3. Summary of the mineral chemistry of examined gabbroic rocks.

Core, section, interval (cm)	Depth (mbsf)	Plagioclase (An)	Olivine (Fo)	Clinopyroxene (Mg#)
176-735B-				
101R-1 (Piece 7, 106–108)	586.16	54.8, 59.7–47.9, *n* = 54	70.3, 72.3–68.1, *n* = 16	81.1, 82.4–79.0, *n* = 8
112R-2 (Piece 1, 64–66)	644.62	52.3, 56.5–45.5, *n* = 5	63.6, 64.4–61.6, *n* = 4	78.4, 83.0–72.8, *n* = 14
130R-3 (Piece 11, 93–95)	797.57	50.1, 53.3–45.6, *n* = 16	64.5, 65.6–64.0, *n* = 8	74.7, 78.2–72.2, *n* = 6
156R-3 (Piece 5, 51–54)	1027.59	53.9, 55.4–52.7, *n* = 11	69.2, 70.3–68.2, *n* = 7	78.8, 80.7–77.1, *n* = 22

Notes: Mineral compositions are average, range, and number of analyses. Plag = plagioclase, Ol = olivine, Cpx = clinopyroxene. An = 100 × Ca/(Ca+Na), Fo = Mg# = 100 × Mg/(Mg+Fe).

Table T4. Selected microprobe analyses of plagioclase, Hole 735B. (Continued on next page.)

Core, section, interval (cm):	101R-1 (Piece 7, 106–108)											112R-2 (Piece 1, 64–66)		
Lithology:	Olivine gabbro											Olivine gabbro		
Texture:	M	M	M	M	M	V	V	V	V	V	V	M	M	M
SiO_2	53.16	54.13	54.05	54.48	53.49	54.60	55.60	58.77	58.69	61.36	61.47	54.11	55.76	56.88
TiO_2	0.03	0.07	0.08	0.04	0.00	0.01	0.02	0.00	0.01	0.01	0.01	0.04	0.09	0.02
Al_2O_3	29.39	29.29	29.09	28.96	29.70	29.09	28.20	26.53	25.90	24.69	24.53	28.62	27.76	27.31
FeO*	0.17	0.15	0.11	0.11	0.04	0.26	0.25	0.15	0.05	0.10	0.07	0.19	0.33	0.17
MnO	0.01	0.01	0.00	0.00	0.00	0.02	0.01	0.01	0.00	0.00	0.01	0.00	0.00	0.00
MgO	0.02	0.02	0.01	0.01	0.00	0.00	0.00	0.00	0.00	0.00	0.02	0.04	0.04	0.01
CaO	12.34	11.76	11.22	10.72	11.37	10.96	9.87	8.06	7.20	6.08	5.59	11.51	10.33	9.54
Na_2O	4.75	5.00	5.16	5.55	5.13	5.38	6.36	7.21	7.66	8.53	8.74	4.90	5.88	6.32
K_2O	0.04	0.04	0.07	0.06	0.01	0.02	0.01	0.03	0.01	0.09	0.11	0.05	0.08	0.04
Cr_2O_3	0.01	0.00	0.00	0.00	0.00	0.00	0.00	0.00	0.00	0.00	0.00	0.01	0.00	0.01
NiO	0.00	0.01	0.02	0.00	0.00	0.00	0.02	0.03	0.05	0.00	0.00	0.00	0.00	0.00
Total	99.91	100.47	99.81	99.93	99.74	100.35	100.35	100.78	99.56	100.86	100.54	99.46	100.26	100.30
Cations (O = 8):														
Si	2.411	2.436	2.445	2.459	2.422	2.456	2.498	2.608	2.632	2.707	2.718	2.457	2.508	2.548
Ti	0.001	0.002	0.003	0.001	0.000	0.000	0.001	0.000	0.000	0.000	0.000	0.001	0.003	0.001
Al	1.571	1.553	1.551	1.541	1.585	1.542	1.493	1.388	1.369	1.284	1.278	1.532	1.471	1.442
Fe	0.006	0.006	0.004	0.004	0.002	0.010	0.009	0.005	0.002	0.004	0.003	0.007	0.012	0.006
Mn	0.000	0.000	0.000	0.000	0.000	0.001	0.000	0.000	0.000	0.000	0.000	0.000	0.000	0.000
Mg	0.001	0.001	0.001	0.001	0.000	0.000	0.000	0.000	0.000	0.000	0.001	0.003	0.002	0.000
Ca	0.600	0.567	0.544	0.518	0.551	0.528	0.475	0.383	0.346	0.288	0.265	0.560	0.498	0.458
Na	0.418	0.436	0.452	0.485	0.451	0.469	0.554	0.621	0.666	0.730	0.749	0.431	0.513	0.549
K	0.002	0.003	0.004	0.004	0.000	0.001	0.001	0.002	0.000	0.005	0.006	0.003	0.005	0.002
Cr	0.000	0.000	0.000	0.000	0.000	0.000	0.000	0.000	0.000	0.000	0.000	0.000	0.000	0.000
Ni	0.000	0.000	0.001	0.000	0.000	0.000	0.001	0.001	0.002	0.000	0.000	0.000	0.000	0.000
Total	5.012	5.004	5.005	5.014	5.011	5.008	5.032	5.009	5.016	5.017	5.020	4.993	5.012	5.006
An	58.9	56.5	54.6	51.6	55.0	53.0	46.2	38.2	34.2	28.3	26.1	56.5	49.3	45.5

Notes: M = magmatic, V = vein. FeO* = total iron as FeO. An = 100 × Ca/(Ca+Na).

Table T4 (continued).

Core, section, interval (cm):	130R-3 (Piece 11, 93–95)							156R-3 (Piece 5, 51–54)					
Lithology:	Olivine gabbro							Olivine gabbro					
Texture:	M	N	M	V	V	V	V	M	M	M	V	V	V
SiO_2	54.22	54.54	56.20	54.91	55.92	57.15	59.37	54.21	54.47	54.96	60.00	59.81	60.93
TiO_2	0.06	0.05	0.05	0.01	0.02	0.04	0.04	0.03	0.07	0.03	0.02	0.02	0.02
Al_2O_3	28.87	28.65	27.20	28.68	27.86	26.99	25.99	28.77	28.53	28.23	24.97	24.62	24.41
FeO*	0.26	0.24	0.28	0.67	0.70	0.46	0.16	0.20	0.12	0.18	0.17	0.28	0.29
MnO	0.01	0.01	0.00	0.01	0.01	0.00	0.01	0.00	0.00	0.00	0.00	0.00	0.00
MgO	0.04	0.02	0.04	0.02	0.09	0.02	0.00	0.02	0.01	0.00	0.01	0.01	0.01
CaO	11.27	11.05	9.58	11.05	9.99	8.31	7.53	11.60	11.26	10.94	7.09	6.86	6.43
Na_2O	5.45	5.46	6.27	5.53	6.13	6.42	7.55	5.16	5.30	5.42	7.63	7.85	8.13
K_2O	0.08	0.08	0.09	0.00	0.01	0.04	0.10	0.06	0.08	0.08	0.07	0.19	0.08
Cr_2O_3	0.00	0.00	0.00	0.00	0.00	0.00	0.00	0.00	0.00	0.00	0.00	0.00	0.00
NiO	0.00	0.00	0.01	0.02	0.00	0.01	0.05	0.00	0.01	0.00	0.01	0.02	0.00
Total	100.27	100.11	99.72	100.88	100.73	99.44	100.80	100.04	99.84	99.83	99.97	99.64	100.29
Cations (O = 8):													
Si	2.447	2.462	2.536	2.463	2.506	2.574	2.633	2.450	2.464	2.484	2.676	2.680	2.706
Ti	0.002	0.002	0.002	0.000	0.001	0.001	0.001	0.001	0.002	0.001	0.001	0.001	0.001
Al	1.536	1.524	1.447	1.516	1.472	1.433	1.359	1.533	1.521	1.503	1.313	1.301	1.278
Fe	0.010	0.009	0.010	0.025	0.026	0.017	0.006	0.008	0.005	0.007	0.006	0.011	0.011
Mn	0.000	0.000	0.000	0.000	0.000	0.000	0.000	0.000	0.000	0.000	0.000	0.000	0.000
Mg	0.003	0.002	0.003	0.001	0.006	0.001	0.000	0.001	0.000	0.000	0.001	0.000	0.001
Ca	0.545	0.534	0.463	0.531	0.480	0.401	0.358	0.562	0.546	0.529	0.339	0.329	0.306
Na	0.477	0.478	0.549	0.481	0.533	0.560	0.649	0.452	0.465	0.475	0.659	0.682	0.700
K	0.005	0.005	0.005	0.000	0.001	0.002	0.006	0.003	0.005	0.005	0.004	0.011	0.004
Cr	0.000	0.000	0.000	0.000	0.000	0.000	0.000	0.000	0.000	0.000	0.000	0.000	0.000
Ni	0.000	0.000	0.001	0.001	0.000	0.000	0.002	0.000	0.000	0.000	0.000	0.001	0.000
Total	5.024	5.016	5.016	5.019	5.024	4.990	5.014	5.010	5.008	5.004	4.999	5.015	5.006
An	53.3	52.8	45.8	52.5	47.4	41.7	35.5	55.4	54.0	52.7	33.9	32.6	30.4

Table T5. Selected microprobe analyses of olivine, Hole 735B.

Core, section, interval (cm):	101R-1 (Piece 7, 106–108)		112R-2 (Piece 1, 64–66)		130R-3 (Piece 11, 93–95)		156R-3 (Piece 5, 51–54)	
Lithology:	Olivine gabbro		Olivine gabbro		Olivine gabbro		Olivine gabbro	
SiO_2	38.32	37.72	37.38	37.57	37.09	36.95	37.81	38.09
TiO_2	0.00	0.01	0.01	0.00	0.01	0.01	0.00	0.02
Al_2O_3	0.01	0.00	0.00	0.01	0.01	0.00	0.00	0.00
FeO*	25.42	27.28	31.64	31.94	30.86	31.64	27.42	26.77
MnO	0.41	0.46	0.57	0.55	0.54	0.50	0.45	0.43
MgO	36.21	35.11	32.04	31.81	31.69	31.61	35.16	35.51
CaO	0.01	0.02	0.01	0.01	0.01	0.03	0.02	0.00
Na_2O	0.00	0.01	0.02	0.01	0.02	0.04	0.00	0.02
K_2O	0.00	0.00	0.00	0.00	0.00	0.00	0.00	0.00
Cr_2O_3	0.00	0.00	0.00	0.00	0.00	0.01	0.00	0.00
NiO	0.09	0.03	0.04	0.03	0.02	0.00	0.07	0.01
Total	100.45	100.64	101.69	101.92	100.27	100.79	100.93	100.85
Cations (O = 4):								
Si	1.006	0.999	1.000	1.003	1.004	0.999	0.999	1.003
Ti	0.000	0.000	0.000	0.000	0.000	0.000	0.000	0.000
Al	0.000	0.000	0.000	0.000	0.000	0.000	0.000	0.000
Fe	0.558	0.604	0.708	0.713	0.699	0.715	0.606	0.590
Mn	0.009	0.010	0.013	0.012	0.012	0.012	0.010	0.010
Mg	1.418	1.386	1.278	1.266	1.279	1.273	1.385	1.394
Ca	0.000	0.000	0.000	0.000	0.000	0.001	0.001	0.000
Na	0.000	0.000	0.001	0.000	0.001	0.002	0.000	0.001
K	0.000	0.000	0.000	0.000	0.000	0.000	0.000	0.000
Cr	0.000	0.000	0.000	0.000	0.000	0.000	0.000	0.000
Ni	0.002	0.001	0.001	0.001	0.000	0.000	0.002	0.000
Total	2.994	3.001	3.000	2.997	2.996	3.002	3.001	2.997
Fo	71.7	69.6	64.4	64.0	64.7	64.0	69.6	70.3

Notes: FeO* = total iron as FeO. Fo = 100 × Mg/(Mg+Fe).

Table T6. Selected microprobe analyses of clinopyroxene, Hole 735B. (Continued on next page.)

Core, section, interval (cm):	101R-1 (Piece 7, 106–108)						112R-2 (Piece 1, 64–66)								
Lithology:	Olivine gabbro						Olivine gabbro								
Texture:	M	M	M	V	V	V	M	M	M	V	V	V	If	If	If
SiO_2	52.59	52.06	52.43	53.11	53.05	53.38	52.31	52.10	52.02	52.19	52.68	53.02	52.63	53.03	51.97
TiO_2	0.57	0.69	0.58	0.25	0.22	0.21	0.67	0.84	0.66	0.64	0.46	0.42	0.64	0.53	0.80
$Al2O_3$	2.96	2.95	3.00	1.45	0.85	0.74	3.14	2.62	3.31	2.12	1.67	1.54	1.96	1.62	2.70
FeO*	8.12	7.30	6.12	6.94	9.11	8.65	6.46	7.48	6.14	8.46	8.17	8.50	8.37	8.37	7.82
MnO	0.25	0.24	0.18	0.28	0.36	0.34	0.18	0.23	0.17	0.27	0.33	0.31	0.26	0.28	0.25
MgO	17.16	16.75	16.02	14.94	14.42	14.47	16.65	15.07	15.34	14.25	14.43	14.55	14.45	14.57	14.52
CaO	17.70	19.04	21.05	21.67	20.60	21.15	20.34	21.46	21.90	21.53	22.01	21.42	21.75	21.76	21.65
Na_2O	0.52	0.42	0.40	0.47	0.41	0.36	0.39	0.37	0.45	0.41	0.36	0.45	0.33	0.37	0.38
K_2O	0.00	0.00	0.00	0.01	0.00	0.00	0.00	0.02	0.00	0.00	0.00	0.00	0.00	0.01	0.01
Cr_2O_3	0.07	0.07	0.10	0.06	0.03	0.03	0.06	0.01	0.09	0.02	0.00	0.00	0.02	0.01	0.04
NiO	0.05	0.00	0.04	0.00	0.02	0.00	0.01	0.00	0.00	0.01	0.03	0.00	0.00	0.03	0.05
Total	99.98	99.51	99.92	99.17	99.08	99.33	100.21	100.20	100.07	99.89	100.13	100.21	100.40	100.58	100.19
Cations (O = 6):															
Si	1.931	1.922	1.927	1.977	1.991	1.995	1.916	1.925	1.914	1.944	1.956	1.966	1.948	1.959	1.925
Ti	0.016	0.019	0.016	0.007	0.006	0.006	0.018	0.023	0.018	0.018	0.013	0.012	0.018	0.015	0.022
Al	0.128	0.128	0.130	0.064	0.038	0.033	0.136	0.114	0.144	0.093	0.073	0.067	0.085	0.070	0.118
Fe	0.249	0.225	0.188	0.216	0.286	0.270	0.198	0.231	0.189	0.264	0.254	0.264	0.259	0.259	0.242
Mn	0.008	0.007	0.006	0.009	0.011	0.011	0.006	0.007	0.005	0.008	0.010	0.010	0.008	0.009	0.008
Mg	0.939	0.922	0.878	0.829	0.807	0.806	0.909	0.830	0.842	0.791	0.799	0.804	0.798	0.802	0.802
Ca	0.696	0.753	0.829	0.864	0.828	0.847	0.798	0.850	0.864	0.859	0.876	0.851	0.863	0.861	0.859
Na	0.037	0.030	0.029	0.034	0.030	0.026	0.028	0.026	0.032	0.029	0.026	0.032	0.023	0.026	0.027
K	0.000	0.000	0.000	0.001	0.000	0.000	0.000	0.001	0.000	0.000	0.000	0.000	0.000	0.000	0.001
Cr	0.002	0.002	0.003	0.002	0.001	0.001	0.002	0.000	0.003	0.001	0.000	0.000	0.001	0.000	0.001
Ni	0.002	0.000	0.001	0.000	0.001	0.000	0.000	0.000	0.000	0.000	0.001	0.000	0.000	0.001	0.001
Total	4.007	4.009	4.005	4.001	3.998	3.995	4.011	4.008	4.010	4.006	4.007	4.005	4.003	4.004	4.007
Mg#	79.03	80.34	82.36	79.33	73.83	74.89	82.13	78.21	81.67	75.00	75.89	75.32	75.48	75.62	76.81
Wo	36.9	39.6	43.8	45.3	43.1	44.0	41.9	44.5	45.6	44.9	45.4	44.3	44.9	44.8	45.1
En	49.8	48.5	46.3	43.4	42.0	41.9	47.7	43.4	44.4	41.3	41.4	41.9	41.6	41.7	42.1
Fs	13.2	11.9	9.9	11.3	14.9	14.1	10.4	12.1	10.0	13.8	13.2	13.7	13.5	13.5	12.7

Notes: M = magmatic, V = near vein. If = interfingering part. FeO* = total iron as FeO. Mg# = 100 × Mg/(Mg+Fe), Wo = 100 × Ca/(Ca+Mg+Fe), En = 100 × Mg/(Ca+Mg+Fe), Fs = 100 × Fe/(Ca+Mg+Fe).

Table T6 (continued).

Core, section, interval (cm):	130R-3 (Piece 11, 93–95)			156R-3 (Piece 5, 5154)								
Lithology:	Olivine gabbro			Olivine gabbro								
Texture:	M	M	M	M	M	M	If	If	If	V	V	V
SiO_2	51.79	52.20	53.04	51.89	51.52	52.19	51.96	52.35	52.36	53.43	52.97	52.31
TiO_2	0.98	0.65	0.43	0.64	0.68	0.64	0.69	0.60	0.71	0.27	0.31	0.54
Al_2O_3	2.69	2.28	1.62	2.69	2.91	2.46	2.48	2.00	2.27	0.85	1.57	2.29
FeO*	8.97	8.49	8.94	7.02	7.22	7.23	7.04	7.17	7.93	6.92	6.32	6.46
MnO	0.31	0.29	0.33	0.23	0.25	0.21	0.23	0.21	0.23	0.29	0.24	0.21
MgO	14.07	14.59	14.35	14.99	15.03	15.03	15.17	15.35	15.69	15.07	14.95	15.52
CaO	20.61	21.31	21.26	21.72	21.01	22.11	21.78	21.71	20.63	22.65	22.88	22.03
Na_2O	0.58	0.35	0.48	0.39	0.52	0.44	0.42	0.37	0.39	0.47	0.44	0.58
K_2O	0.00	0.00	0.00	0.00	0.00	0.00	0.00	0.00	0.00	0.01	0.00	0.01
Cr_2O_3	0.00	0.00	0.01	0.03	0.03	0.03	0.02	0.01	0.01	0.02	0.03	0.02
NiO	0.00	0.01	0.00	0.00	0.00	0.03	0.01	0.00	0.00	0.00	0.00	0.00
Total	100.01	100.18	100.44	99.59	99.18	100.37	99.80	99.78	100.20	99.96	99.71	99.96
Cations (O = 6):												
Si	1.928	1.937	1.965	1.927	1.921	1.927	1.927	1.941	1.933	1.979	1.963	1.933
Ti	0.028	0.018	0.012	0.018	0.019	0.018	0.019	0.017	0.020	0.007	0.009	0.015
Al	0.118	0.100	0.071	0.118	0.128	0.107	0.108	0.087	0.099	0.037	0.069	0.100
Fe	0.279	0.263	0.277	0.218	0.225	0.223	0.218	0.222	0.245	0.214	0.196	0.200
Mn	0.010	0.009	0.010	0.007	0.008	0.007	0.007	0.007	0.007	0.009	0.008	0.007
Mg	0.780	0.807	0.792	0.830	0.835	0.827	0.839	0.849	0.864	0.832	0.826	0.855
Ca	0.822	0.847	0.844	0.864	0.839	0.875	0.865	0.862	0.816	0.899	0.908	0.872
Na	0.042	0.025	0.034	0.028	0.038	0.031	0.030	0.026	0.028	0.034	0.031	0.041
K	0.000	0.000	0.000	0.000	0.000	0.000	0.000	0.000	0.000	0.000	0.000	0.000
Cr	0.000	0.000	0.000	0.001	0.001	0.001	0.001	0.000	0.000	0.000	0.001	0.001
Ni	0.000	0.000	0.000	0.000	0.000	0.001	0.000	0.000	0.000	0.000	0.000	0.000
Total	4.007	4.007	4.005	4.010	4.014	4.017	4.015	4.012	4.011	4.012	4.010	4.023
Mg#	73.65	75.39	74.11	79.18	78.77	78.74	79.36	79.23	77.91	79.51	80.83	81.08
Wo	43.7	44.2	44.10	45.2	44.2	45.4	45.0	44.6	42.4	46.2	47.1	45.3
En	41.5	42.1	41.42	43.4	44.0	43.0	43.6	43.9	44.9	42.8	42.8	44.4
Fs	14.8	13.7	14.47	11.4	11.9	11.6	11.4	11.5	12.7	11.0	10.1	10.4

Table T7. Selected microprobe analyses of orthopyroxene, Hole 735B. (Continued on next page.)

Core, section, interval (cm):	101R-1 (Piece 7, 106–108)				112R-2 (Piece 1, 64–66)							
Lithology:	Olivine gabbro				Olivine gabbro							
Texture:	VOl	VOl	VOl	VOl	M	M	Blf	Blf	Blf	BV	BV	BV
SiO_2	55.01	55.15	55.33	54.47	54.35	54.10	53.71	53.70	53.67	53.52	53.62	53.95
TiO_2	0.14	0.08	0.11	0.01	0.15	0.13	0.26	0.30	0.35	0.27	0.34	0.19
Al_2O_3	0.50	1.03	0.58	1.22	0.96	1.11	0.68	0.70	1.48	0.75	1.00	0.78
FeO*	16.43	16.17	16.47	16.58	18.39	18.21	21.49	20.94	18.56	20.89	20.08	21.25
MnO	0.51	0.47	0.45	0.40	0.45	0.49	0.61	0.64	0.47	0.58	0.56	0.58
MgO	26.85	27.27	26.88	27.45	25.50	24.96	22.34	22.67	24.58	22.82	23.33	22.35
CaO	0.83	0.34	0.79	0.27	0.96	0.91	1.04	1.09	1.09	1.16	1.35	1.57
Na_2O	0.00	0.01	0.00	0.00	0.03	0.02	0.00	0.00	0.04	0.01	0.02	0.03
K_2O	0.00	0.00	0.00	0.00	0.00	0.00	0.01	0.00	0.00	0.01	0.00	0.00
Cr_2O_3	0.00	0.00	0.00	0.00	0.01	0.01	0.00	0.00	0.02	0.00	0.00	0.00
NiO	0.01	0.02	0.03	0.01	0.02	0.04	0.00	0.03	0.01	0.00	0.00	0.01
Total	100.28	100.54	100.64	100.40	100.82	99.98	100.12	100.08	100.26	100.01	100.30	100.70
Cations (O = 6):												
Si	1.986	1.979	1.989	1.962	1.971	1.976	1.990	1.987	1.960	1.982	1.974	1.988
Ti	0.004	0.002	0.003	0.000	0.004	0.003	0.007	0.008	0.009	0.007	0.009	0.005
Al	0.021	0.044	0.024	0.052	0.041	0.048	0.030	0.031	0.064	0.033	0.043	0.034
Fe	0.496	0.485	0.495	0.500	0.558	0.556	0.666	0.648	0.567	0.647	0.618	0.655
Mn	0.016	0.014	0.014	0.012	0.014	0.015	0.019	0.020	0.015	0.018	0.018	0.018
Mg	1.445	1.459	1.440	1.475	1.378	1.359	1.234	1.250	1.338	1.260	1.280	1.228
Ca	0.032	0.013	0.030	0.011	0.037	0.036	0.041	0.043	0.043	0.046	0.053	0.062
Na	0.000	0.001	0.000	0.000	0.002	0.001	0.000	0.000	0.003	0.000	0.002	0.002
K	0.000	0.000	0.000	0.000	0.000	0.000	0.000	0.000	0.000	0.000	0.000	0.000
Cr	0.000	0.000	0.000	0.000	0.000	0.000	0.000	0.000	0.000	0.000	0.000	0.000
Ni	0.000	0.000	0.001	0.000	0.001	0.001	0.000	0.001	0.000	0.000	0.000	0.000
Total	4.000	3.997	3.996	4.012	4.006	3.997	3.988	3.989	3.999	3.994	3.996	3.991
Mg#	74.4	75.0	74.4	74.7	71.2	71.0	65.0	65.9	70.2	66.1	67.4	65.2
Wo	1.6	0.7	1.5	0.5	1.9	1.8	2.1	2.2	2.2	2.4	2.7	3.2
En	73.2	74.5	73.3	74.3	69.9	69.7	63.6	64.4	68.7	64.5	65.6	63.1
Fs	25.1	24.8	25.2	25.2	28.3	28.5	34.3	33.4	29.1	33.1	31.7	33.7

Notes: M = magmatic rim, VOl = vein in olivine, Blf = bleb in interfingering clinopyroxene, BV = bleb near vein. FeO* = total iron as FeO. Mg# = 100 × Mg/(Mg+Fe), Wo = 100 × Ca/(Ca+Mg+Fe), En = 100 × Mg/(Ca+Mg+Fe), Fs = 100 × Fe/(Ca+Mg+Fe).

Table T7 (continued).

Core, section, interval (cm):	130R-3 (Piece 11, 93–95)						156R-3 (Piece 5, 51–54)						
Lithology:	Olivine gabbro						Olivine gabbro						
Texture:	M	M	VOl	VOl	BV	BV	M	M	M	BIf	BIf	BIf	BV
SiO_2	53.54	54.42	54.01	54.09	53.40	52.75	54.09	54.26	54.05	53.99	53.74	53.89	53.93
TiO_2	0.36	0.11	0.24	0.11	0.20	0.13	0.35	0.37	0.33	0.32	0.35	0.25	0.10
Al_2O_3	1.25	0.76	1.58	1.04	0.66	0.55	1.32	1.31	1.26	1.15	1.23	1.06	0.33
FeO*	18.68	18.04	18.44	18.21	21.10	22.87	16.27	16.44	16.34	17.26	17.32	17.35	19.76
MnO	0.47	0.52	0.46	0.49	0.51	0.53	0.40	0.39	0.42	0.40	0.46	0.42	0.55
MgO	24.14	25.41	24.63	25.12	22.55	21.27	26.17	26.41	26.24	25.49	25.46	25.45	24.04
CaO	1.58	0.55	1.02	0.36	1.01	0.94	1.27	1.30	1.22	1.19	1.21	0.98	0.74
Na_2O	0.02	0.01	0.00	0.00	0.03	0.02	0.02	0.01	0.00	0.04	0.01	0.01	0.00
K_2O	0.00	0.00	0.00	0.00	0.01	0.01	0.00	0.00	0.00	0.00	0.01	0.00	0.00
Cr_2O_3	0.00	0.00	0.00	0.00	0.01	0.01	0.00	0.00	0.00	0.01	0.02	0.01	0.00
NiO	0.03	0.01	0.00	0.02	0.03	0.03	0.07	0.02	0.00	0.00	0.01	0.00	0.04
Total	100.07	99.82	100.38	99.45	99.50	99.10	99.96	100.51	99.87	99.84	99.82	99.42	99.48
Cations (O = 6):													
Si	1.964	1.987	1.967	1.983	1.989	1.990	1.962	1.958	1.962	1.968	1.962	1.973	1.995
Ti	0.010	0.003	0.006	0.003	0.006	0.004	0.010	0.010	0.054	0.009	0.010	0.007	0.003
Al	0.054	0.033	0.068	0.045	0.029	0.024	0.057	0.056	0.009	0.049	0.053	0.046	0.014
Fe	0.573	0.551	0.561	0.558	0.657	0.722	0.494	0.496	0.496	0.526	0.529	0.531	0.611
Mn	0.015	0.016	0.014	0.015	0.016	0.017	0.012	0.012	0.013	0.012	0.014	0.013	0.017
Mg	1.320	1.383	1.337	1.373	1.252	1.197	1.415	1.421	1.420	1.385	1.386	1.389	1.325
Ca	0.062	0.021	0.040	0.014	0.040	0.038	0.049	0.050	0.047	0.047	0.047	0.039	0.029
Na	0.001	0.001	0.000	0.000	0.002	0.001	0.001	0.001	0.000	0.003	0.000	0.001	0.000
K	0.000	0.000	0.000	0.000	0.000	0.000	0.000	0.000	0.000	0.000	0.000	0.000	0.000
Cr	0.000	0.000	0.000	0.000	0.000	0.000	0.000	0.000	0.000	0.000	0.001	0.000	0.000
Ni	0.001	0.000	0.000	0.001	0.001	0.001	0.002	0.001	0.000	0.000	0.000	0.000	0.001
Total	4.000	3.994	3.993	3.992	3.992	3.995	4.001	4.004	4.002	4.000	4.002	3.998	3.996
Mg#	69.7	71.5	70.4	71.1	65.6	62.4	74.1	74.1	74.1	72.5	72.4	72.3	68.4
Wo	3.2	1.1	2.1	0.7	2.1	1.9	2.5	2.6	2.4	2.4	2.4	2.0	1.5
En	67.5	70.7	69.0	70.6	64.2	61.2	72.3	72.2	72.3	70.7	70.6	70.9	67.4
Fs	29.3	28.2	29.0	28.7	33.7	36.9	25.2	25.2	25.3	26.9	27.0	27.1	31.1

Table T8. Selected microprobe analyses of amphibole, Hole 735B. (Continued on next page.)

Core, section, interval (cm):	101R-1 (Piece 7, 106–108)									112R-2 (Piece 1, 64–66)								
Lithology:	Olivine gabbro									Olivine gabbro								
Texture:	M	M	M	VOl	VOl	VOl	VCpx	VCpx	VCpx	M	M	M	BIf	BIf	BIf	BV	BV	BV
SiO_2	43.90	44.80	42.82	44.05	44.38	45.26	47.53	45.54	46.30	43.27	43.15	41.44	43.73	43.45	44.14	44.16	43.87	44.03
TiO_2	3.41	2.92	2.83	1.11	0.97	0.36	2.12	3.06	2.86	3.46	2.83	0.25	3.39	3.88	2.68	3.72	3.85	3.69
Al_2O_3	11.45	11.88	13.05	13.05	12.80	11.72	8.18	8.77	8.39	11.48	11.65	13.91	10.65	10.75	11.84	10.56	10.19	10.04
Fe_2O_3	0.00	0.00	0.00	0.00	0.00	0.00	0.00	0.00	0.00	0.00	0.00	1.23	0.00	0.00	0.00	0.00	0.00	0.00
FeO	10.38	8.54	9.26	9.17	9.54	8.78	11.11	12.00	11.63	11.87	12.63	15.51	11.78	11.37	8.50	11.83	11.70	12.55
MnO	0.11	0.20	0.14	0.22	0.17	0.17	0.19	0.21	0.18	0.20	0.16	0.20	0.20	0.16	0.12	0.18	0.18	0.17
MgO	14.34	15.63	14.72	15.73	16.14	16.93	15.34	13.99	14.29	13.88	13.42	10.46	13.61	13.72	15.54	13.58	13.71	13.13
CaO	11.73	10.82	11.24	9.97	10.17	10.35	10.91	10.81	11.02	10.85	10.89	11.43	11.31	11.10	11.46	10.98	11.11	11.14
Na_2O	2.74	2.50	2.89	2.67	2.92	2.57	1.89	2.35	2.26	3.01	3.03	2.92	2.90	3.10	2.85	2.90	2.94	2.92
K_2O	0.25	0.24	0.29	0.13	0.25	0.17	0.25	0.33	0.30	0.24	0.23	0.28	0.04	0.05	0.14	0.37	0.21	0.21
Cr_2O_3	0.01	0.04	0.05	0.00	0.00	0.00	0.08	0.13	0.13	0.00	0.00	0.00	0.04	0.06	0.10	0.02	0.02	0.00
NiO	0.06	0.01	0.00	0.04	0.03	0.00	0.00	0.01	0.04	0.00	0.01	0.01	0.01	0.00	0.00	0.00	0.02	0.06
Total	98.36	97.57	97.28	96.15	97.36	97.11	97.58	97.20	97.40	98.25	97.98	97.64	97.64	97.64	97.37	98.29	97.79	97.94
Cations (O = 23):																		
Si	6.360	6.448	6.240	6.431	6.423	6.543	6.885	6.693	6.770	6.318	6.337	6.220	6.419	6.372	6.391	6.441	6.433	6.470
Al	1.955	2.015	2.240	2.246	2.184	1.996	1.396	1.519	1.446	1.975	2.016	2.460	1.843	1.858	2.020	1.815	1.762	1.739
Al^{IV}	1.640	1.552	1.760	1.569	1.577	1.457	1.115	1.307	1.230	1.682	1.663	1.780	1.581	1.628	1.609	1.559	1.567	1.530
Al^{VI}	0.315	0.462	0.480	0.677	0.607	0.540	0.281	0.212	0.216	0.293	0.353	0.680	0.262	0.230	0.411	0.256	0.195	0.209
Cr	0.001	0.004	0.006	0.000	0.000	0.000	0.009	0.015	0.015	0.000	0.000	0.000	0.004	0.007	0.012	0.002	0.002	0.000
Fe^{3+}	0.000	0.000	0.000	0.000	0.000	0.087	0.000	0.000	0.000	0.000	0.000	0.139	0.000	0.000	0.000	0.000	0.000	0.000
Ti	0.371	0.316	0.310	0.122	0.105	0.040	0.230	0.338	0.314	0.380	0.312	0.028	0.374	0.428	0.291	0.408	0.424	0.408
Fe^{2+}	1.258	1.028	1.128	1.119	1.154	1.061	1.345	1.475	1.422	1.450	1.551	1.947	1.446	1.394	1.029	1.443	1.435	1.542
Mn	0.013	0.024	0.018	0.027	0.020	0.021	0.023	0.026	0.022	0.024	0.020	0.026	0.024	0.020	0.014	0.022	0.022	0.022
Mg	3.097	3.353	3.197	3.424	3.481	3.648	3.313	3.065	3.116	3.021	2.938	2.340	2.977	2.999	3.354	2.953	2.997	2.876
Ni	0.007	0.001	0.000	0.004	0.003	0.000	0.000	0.002	0.005	0.000	0.001	0.001	0.001	0.000	0.000	0.000	0.002	0.007
Ca	1.821	1.668	1.755	1.560	1.577	1.603	1.693	1.703	1.726	1.698	1.714	1.839	1.778	1.744	1.778	1.715	1.746	1.753
Na	0.769	0.698	0.816	0.756	0.819	0.719	0.531	0.669	0.640	0.852	0.864	0.851	0.826	0.882	0.800	0.821	0.835	0.833
K	0.046	0.044	0.054	0.025	0.046	0.031	0.045	0.061	0.057	0.045	0.043	0.053	0.007	0.009	0.027	0.069	0.039	0.039
Total	15.699	15.598	15.763	15.714	15.812	15.750	15.470	15.566	15.534	15.763	15.796	15.904	15.699	15.713	15.715	15.688	15.698	15.689
Mg#	71.1	76.5	73.9	75.4	75.1	77.5	71.1	67.5	68.7	67.6	65.5	54.6	67.3	68.3	76.5	67.2	67.6	65.1

Notes: M = magmatic rim, VOl = vein in olivine, VCpx = vein in clinopyroxene, BIf = bleb in interfingering clinopyroxene, BV = bleb near vein, and Mg# = 100 × Mg/(Mg + Fe). See "Appendix," p. 20, for procedures of formula calculation.

Table T8 (continued).

Core, section, interval (cm):	130R-3 (Piece 11, 93–95)								156R-3 (Piece 5, 51–54)										
Lithology:	Olivine gabbro								Olivine gabbro										
Texture:	M	M	M	VOl	VOl	VCpx	VCpx	VCpx	M	M	BIf	BIf	BIf	BV	BV	BV	VCpx	VCpx	VCpx
SiO_2	43.06	44.06	42.85	43.25	44.00	53.19	50.89	51.79	46.51	44.80	43.45	43.95	44.22	46.61	49.26	46.20	46.72	48.43	46.42
TiO_2	3.82	2.62	3.52	0.37	0.53	0.83	1.23	1.03	0.40	0.43	3.19	3.04	2.99	2.39	1.53	1.92	1.97	1.40	2.30
Al_2O_3	10.79	11.86	10.87	13.01	12.69	3.16	4.80	3.95	9.79	11.69	11.04	10.72	10.11	8.07	6.08	8.79	7.91	7.08	8.17
Fe_2O_3	0.00	0.00	0.00	1.24	1.06	0.00	0.00	0.00	1.49	0.95	0.00	0.00	0.00	0.00	0.00	0.00	0.00	0.00	0.00
FeO	12.47	10.52	13.22	9.94	10.28	11.53	11.66	11.01	8.86	8.93	10.26	10.05	10.36	10.48	9.55	10.08	11.74	11.17	11.58
MnO	0.20	0.14	0.20	0.20	0.18	0.23	0.21	0.19	0.24	0.11	0.14	0.08	0.16	0.17	0.15	0.11	0.17	0.18	0.17
MgO	13.26	13.84	12.69	15.06	15.18	17.16	16.73	16.56	16.23	15.63	14.48	14.68	14.79	15.25	16.63	15.64	14.67	15.58	14.64
CaO	10.83	11.68	10.90	10.82	10.91	10.93	11.62	11.30	11.27	11.46	11.73	11.80	11.81	11.64	12.14	11.70	11.62	11.52	11.77
Na_2O	2.90	2.39	2.80	2.97	2.82	0.93	1.29	1.17	1.91	2.32	2.84	2.69	2.76	2.18	1.68	2.22	2.01	1.70	2.10
K_2O	0.22	0.26	0.22	0.07	0.10	0.06	0.16	0.18	0.22	0.31	0.10	0.13	0.07	0.40	0.19	0.24	0.30	0.23	0.31
Cr_2O_3	0.02	0.02	0.03	0.00	0.00	0.02	0.01	0.02	0.00	0.01	0.07	0.05	0.03	0.12	0.06	0.06	0.06	0.03	0.06
NiO	0.01	0.03	0.00	0.03	0.04	0.00	0.00	0.01	0.04	0.03	0.00	0.03	0.00	0.02	0.00	0.03	0.00	0.02	0.03
Total	97.56	97.41	97.29	96.96	97.79	98.04	98.58	97.21	96.95	96.66	97.30	97.23	97.31	97.33	97.26	96.99	97.15	97.33	97.57
Cations (O = 23):																			
Si	6.353	6.429	6.362	6.339	6.392	7.584	7.280	7.466	6.749	6.538	6.366	6.429	6.475	6.797	7.113	6.743	6.850	7.032	6.785
Al	1.877	2.040	1.902	2.248	2.172	0.531	0.809	0.671	1.675	2.011	1.906	1.849	1.745	1.387	1.034	1.512	1.367	1.212	1.407
Al^{IV}	1.647	1.571	1.638	1.661	1.608	0.416	0.720	0.534	1.251	1.462	1.634	1.571	1.525	1.203	0.887	1.257	1.150	0.968	1.215
Al^{VI}	0.230	0.469	0.264	0.587	0.565	0.115	0.089	0.137	0.424	0.549	0.272	0.279	0.221	0.184	0.147	0.254	0.217	0.244	0.192
Cr	0.002	0.002	0.003	0.000	0.000	0.002	0.001	0.002	0.000	0.001	0.008	0.006	0.004	0.013	0.006	0.007	0.006	0.004	0.007
Fe^{3+}	0.000	0.000	0.000	0.137	0.116	0.000	0.000	0.000	0.163	0.105	0.000	0.000	0.000	0.000	0.000	0.000	0.000	0.000	0.000
Ti	0.423	0.288	0.393	0.041	0.057	0.089	0.132	0.111	0.043	0.047	0.352	0.335	0.329	0.262	0.167	0.210	0.217	0.153	0.253
Fe^{2+}	1.538	1.284	1.641	1.218	1.249	1.374	1.395	1.327	1.075	1.090	1.257	1.230	1.269	1.278	1.153	1.230	1.440	1.356	1.416
Mn	0.025	0.017	0.025	0.024	0.022	0.028	0.025	0.024	0.030	0.013	0.017	0.010	0.020	0.021	0.018	0.014	0.021	0.023	0.021
Mg	2.917	3.011	2.809	3.291	3.287	3.648	3.567	3.558	3.510	3.400	3.164	3.203	3.228	3.316	3.580	3.402	3.207	3.372	3.190
Ni	0.001	0.003	0.000	0.003	0.005	0.000	0.000	0.001	0.004	0.003	0.000	0.003	0.000	0.003	0.000	0.003	0.000	0.003	0.004
Ca	1.712	1.826	1.735	1.699	1.698	1.670	1.781	1.745	1.752	1.792	1.842	1.850	1.853	1.818	1.878	1.829	1.825	1.792	1.843
Na	0.830	0.675	0.807	0.843	0.794	0.258	0.358	0.328	0.536	0.656	0.807	0.763	0.783	0.617	0.471	0.629	0.570	0.478	0.596
K	0.040	0.049	0.041	0.013	0.018	0.012	0.028	0.034	0.041	0.057	0.019	0.024	0.014	0.075	0.034	0.045	0.056	0.043	0.059
Total	15.719	15.624	15.717	15.856	15.812	15.196	15.376	15.267	15.577	15.713	15.738	15.702	15.720	15.587	15.453	15.625	15.560	15.468	15.582
Mg#	65.5	70.1	63.1	73.0	72.5	72.6	71.9	72.8	76.6	75.7	71.6	72.3	71.8	72.2	75.6	73.4	69.0	71.3	69.3

Table T9. Occurrence of the interfingering texture of clinopyroxene.

	Troctolite	Olivine gabbro and gabbro	Oxide-rich gabbros	Microgabbros	Felsic veins	All samples
Presence (typical)	0 (0.0%)	116 (70.3%)	0 (0.0%)	0 (0.0%)	0 (0.0%)	116 (53.5%)
Presence (not very typical)	0 (0.0%)	18 (10.9%)	1 (6.3%)	0 (0.0%)	0 (0.0%)	19 (8.8%)
Absence	11 (100.0%)	31 (18.8%)	15 (93.8%)	24 (100.0%)	1 (100.0%)	82 (37.8%)
Total	11	165	16	24	1	217

Table T10. Summary of the calculated temperatures, Hole 735B.

Core, section, interval (cm)	Type	Temperature (°C)			Standard deviation	*N*
		Maximum	Minimum	Average		
101R-1 (Piece 7, 106–108)						
Mineral						
Clinopyroxene	Magmatic	1189	912	1041	97	12
Clinopyroxene	Near vein	920	836	871	29	7
Orthopyroxene	Vein in olivine	880	686	786	63	22
Amphibole-plagioclase	Magmatic	880	802	849	26	9
Amphibole-plagioclase	Vein in olivine	821	728	772	37	8
Amphibole-plagioclase	Vein in clinopyroxene	788	741	760	19	6
112R-2 (Piece 1, 64–66)						
Clinopyroxene	Magmatic	1159	811	1016	108	14
Clinopyroxene	Interfinger	984	840	891	45	8
Clinopyroxene	Near vein	931	826	883	35	6
Orthopyroxene	Bleb in interfinger	931	889	912	18	4
Orthopyroxene	Bleb near vein	1004	924	966	40	3
Orthopyroxene	Magmatic rim	902	888	895	10	2
Amphibole-plagioclase	Magmatic	923	776	863	56	9
130R-3 (Piece 11, 93–95)						
Clinopyroxene	Magmatic	1119	892	977	19	9
Orthopyroxene	Magmatic	1031	781	906	177	2
Orthopyroxene	Bleb near vein	891	855	876	11	4
Amphibole-plagioclase	Vein in olivine	914	708	811	146	2
Amphibole-plagioclase	Magmatic	938	809	889	70	3
Amphibole-plagioclase	Vein in olivine	824	822	823	1	2
Amphibole-plagioclase	Vein in clinopyroxene	747	717	731	13	4
156R-3 (Piece 5, 51–54)						
Clinopyroxene	Magmatic	1208	914	997	87	22
Clinopyroxene	Interfinger	1009	915	952	50	3
Clinopyroxene	Near vein	1002	705	807	100	10
Orthopyroxene	Magmatic rim	997	969	982	11	5
Orthopyroxene	Bleb in interfinger	981	914	953	24	6
Orthopyroxene	Bleb near vein	1027	822	892	85	7
Amphibole-plagioclase	Magmatic	792	783	787	6	2
Amphibole-plagioclase	Vein in clinopyroxene	767	653	716	35	10